

Defect Chemistry and Doping of BiCuSeO

Michael Y. Toriyama,^{a*} Jiaxing Qu,^b G. Jeffrey Snyder,^a Prashun Gorai^{c*}

While *p*-type BiCuSeO is a well-known mid-temperature oxide thermoelectric (TE) material, computations predict that superior TE performance can be realized through *n*-type doping. In this study, we use first-principles defect calculations to show that Cu vacancies are responsible for the native *p*-type self doping; yet, we find that BiCuSeO is *n*-type dopable under Cu-rich growth conditions, where the formation of Cu vacancies is suppressed. We computationally survey a broad suite of 23 dopants and find that only Cl and Br are effective *n*-type dopants. Therefore, we recommend that future experimental doping efforts utilize phase boundary mapping to optimize the electron concentration and resolve the anomalous *p*-*n*-*p* transitions observed in halogen-doped BiCuSeO. The prospects of *n*-type doping, as revealed by our defect calculations, paves the path for rational design of BiCuSeO chemical analogues with similar doping behavior and even better TE performance.

1 Introduction

p-type BiCuSeO is one of the most promising thermoelectric (TE) materials for mid-temperature applications,¹ reaching a maximum TE figure of merit (zT) of ~ 1.5 at 823 K when co-doped with Ca and Pb.² The high zT is, in part, due to the high thermopower (~ 350 $\mu\text{V/K}$ at room temperature)¹ as well as the intrinsically low lattice thermal conductivity (< 1 W/mK) arising from its low Young's modulus^{3,4} and strong anharmonicity.⁵ As a result, BiCuSeO has attracted, and continues to inspire, a myriad of studies to further improve its TE performance.^{1,6-8}

Tuning of the charge carrier (hole, electron) concentrations is needed to optimize the *p*- or *n*-type TE performance of materials.⁹ For BiCuSeO, doping efforts have almost exclusively been limited to optimizing the hole carrier concentration because the as-grown material is natively *p*-type. Doping with group-2 elements (Ca, Sr, and Ba) has been successful in optimizing *p*-type BiCuSeO.¹⁰⁻¹³ Other efforts to optimize *p*-type BiCuSeO have included doping with group-1 elements such as Na,¹⁴⁻¹⁶ K,^{17,18} and Cs,¹⁹ converging the light and heavy hole bands through alloying with La,²⁰ and increasing the electrical conductivity via isovalent Ag doping.²¹⁻²³ The widespread success of *p*-type BiCuSeO begs the question of whether BiCuSeO can be doped *n*-type and if it performs equally well as a TE material. We address these questions in this study by computing the formation energies of native defects and 23 dopants in BiCuSeO.

Yang et al.²⁶ have shown, using Boltzmann transport theory calculations, that the zT of *n*-type BiCuSeO can exceed that of *p*-type BiCuSeO due to the low conduction band effective mass. We also perform an independent analysis based on a semi-empirical model for the quality factor (β), which is a measure of the optimized zT ^{24,25,27}

$$\beta \propto \frac{\mu m_{\text{DOS}}^*{}^{3/2}}{\kappa_L} T^{5/2} \quad (1)$$

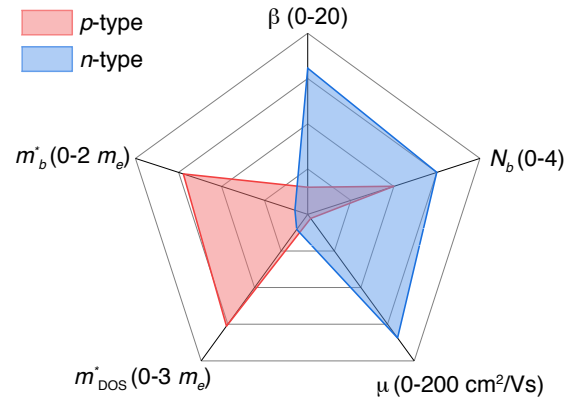


Fig. 1 Comparison of the relevant calculated electronic transport properties of *p*-type (red) and *n*-type (blue) BiCuSeO. β is the predicted thermoelectric performance,^{24,25} μ is the room-temperature mobility in cm^2/Vs , N_b is the band degeneracy, and m_b^* and m_{DOS}^* are the band and density-of-states (DOS) effective masses, respectively, in units of the free electron mass (m_e).

where μ is the intrinsic charge carrier mobility at 300 K, m_{DOS}^* is the density-of-states effective mass, κ_L is the lattice thermal conductivity at 300 K, and T is the temperature. Parameters that are relevant for electronic transport are summarized in Figure 1. Note that κ_L is a common denominator for *p*- and *n*-type β . We calculate a hole mobility of 6 cm^2/Vs , which is in agreement with the range of experimentally-measured Hall mobilities (4 - 22 cm^2/Vs).^{1,28} While m_{DOS}^* is higher for *p*-type BiCuSeO suggesting higher thermopower, the combination of lower band effective mass (m_b^*), corresponding to a higher carrier mobility, and higher band degeneracy (N_b) predicts a higher TE performance for *n*-type BiCuSeO.

While previous experimental studies have attempted to synthesize *n*-type BiCuSeO,²⁹⁻³² none have been able to successfully demonstrate stable *n*-type conductivity. In particular, doping with halogens (Cl, Br, and I) is found to undergo an anomalous *p*-*n*-*p* transition in the carrier type with increasing temperature,

^aNorthwestern University, Evanston, IL 60208. ^bUniversity of Illinois at Urbana-Champaign, Urbana, IL 61801. ^cColorado School of Mines, Golden, CO 80401. *E-mail: michaeltoriyama2024@u.northwestern.edu, pgorai@mines.edu

which has been attributed to the poor thermal stability of the dopants in BiCuSeO.^{30,31} While this unusual behavior was explained in terms of the chemical bonding strength,³¹ it is not entirely clear why *n*-type doping is difficult — is it due to compensating acceptor-like native defects that limit *n*-type doping or the low solubility of dopants? In addition, a broader pool of plausible *n*-type dopants for BiCuSeO remains to be explored.

In this study, we assess the *p*- and *n*-type dopability of BiCuSeO by performing first-principles defect calculations for a comprehensive set of native defects and dopants. We find that BiCuSeO is natively a *p*-type semiconductor, mainly due to the low formation energies of acceptor copper vacancies (V_{Cu}). Interestingly, we also find that BiCuSeO is *n*-type dopable under Cu-rich conditions, when the formation of the electron-compensating V_{Cu} is most suppressed. Despite the possibility of achieving *n*-type BiCuSeO, out of the 23 dopants that are considered in this study, we find that only doping with halogens (Cl, Br) achieve free electron concentrations of $\sim 10^{18} \text{ cm}^{-3}$. Accordingly, while native electron-compensating acceptor defects can be suppressed under appropriate growth conditions, the solubility of dopants is the primary limiting factor to achieving *n*-type conductivity in BiCuSeO. As a result, we stress that thermodynamic growth conditions and the resulting competing impurity phases of doped samples be carefully analyzed when pursuing *n*-type BiCuSeO.

2 Computational Methods

The first-principles density functional theory (DFT) calculations were performed using the Vienna Ab initio Simulation Package (VASP).^{33,34} The core and valence electrons were treated with the projector augmented wave method.^{35,36} The plane-wave energy cutoff was set to 340 eV for all calculations except for dopant calculations involving F, where we instead use a larger cutoff of 540 eV. A rotationally invariant Hubbard U on-site correction³⁷ was applied to Cu ($U = 5 \text{ eV}$).³⁸

2.1 Structure Relaxation

BiCuSeO has ZrSiCuAs-type layered structure with space group $P4/nmm$ (number 129), shown in Figure S1(a). Since BiCuSeO has a layered crystal structure, we found that structure relaxation with the generalized gradient approximation (GGA) of Perdew-Burke-Ernzerhof (PBE)³⁹ overestimated the *c* axis by 1.5% (Table S1 in the supplementary information). It is well known that the GGA functional underbinds the layers in quasi-2D structures such as BiCuSeO due to the absence of long-range van der Waals interactions.⁴⁰ The crystal structure relaxed with the vdW-corrected optB86 exchange-correlation functional (vdW+ U)⁴¹ yielded lattice constants in much better agreement with experimental values ($< 0.1\%$ error; see Table S1) compared to GGA+ U .

2.2 Electronic Structure

The electronic structure of BiCuSeO was calculated using the GGA+ U functional on the crystal structure relaxed using vdW+ U , as suggested by Marom et al.⁴² The electronic structure was calculated using the tetrahedron method for *k*-point integrations,⁴³ using a dense $12 \times 12 \times 6$ Γ -centered *k*-point mesh. It is

well-known that the band gap is underestimated with the GGA functional, which can affect the calculated defect formation energies and charge carrier concentrations. We address the band gap issue by applying shifts to the band edge positions based on GW quasiparticle energy calculations,^{44–48} which resulted in the valence (conduction) band edge shifts of -0.36 (+0.08) eV relative to the GGA band edges. We also included relativistic spin-orbit coupling (SOC) effects due to the presence of heavy Bi atoms, from which we obtained valence (conduction) band edge shifts of +0.02 (-0.31) eV. The “corrected” band gap of 0.88 eV is in close agreement with the experimental value of $\sim 0.8 \text{ eV}$.⁴⁹ The band structure calculated along the high-symmetry *k*-point paths^{50,51} is shown in Figure S2.

2.3 Defect Energetics

The defect energetics were calculated using the standard supercell approach.^{52,53} A $3 \times 3 \times 2$ supercell of BiCuSeO, containing 144 atoms, was considered for all defect formation energy calculations. We calculated the total energies of the host and defect supercells using a two-step process: first, we relaxed the ionic positions using the optB86 vdW-corrected functional with a $3 \times 3 \times 2$ Γ -centered *k*-point mesh, and afterwards calculated the total energy of the vdW-relaxed supercell using a self-consistent GGA+ U calculation with a $6 \times 6 \times 4$ Γ -centered *k*-point mesh.

The formation energies of defects were calculated as

$$\Delta E_{D^q} = E_{D^q} - E_{\text{host}} + \sum_i n_i \mu_i + qE_F + E_{\text{corr}} \quad (2)$$

where ΔE_{D^q} is the formation energy of defect *D* in charge state *q*, E_{D^q} and E_{host} are the total energies of the supercell with and without the defect respectively, and E_F is the Fermi energy.

The chemical potential μ_i of element *i* is expressed relative to a reference state (μ_i^0) such that $\mu_i = \mu_i^0 + \Delta\mu_i$. A certain number of atoms (n_i) of element *i* are added ($n_i < 0$) or removed ($n_i > 0$) from the host supercell to form the defect *D*. The reference chemical potentials μ_i^0 were determined by fitting them to a set of experimentally-measured formation enthalpy^{54,55} (under standard conditions) of several compounds in the Bi-Cu-Se-O quaternary chemical space.^{56–61} The fitted values of μ_i^0 of all elements considered in this study are tabulated in Table S2. The bounds on $\Delta\mu_i$ are set by thermodynamic phase stability conditions; specifically, $\Delta\mu_i$ should satisfy the constraint $\Delta\mu_{\text{Bi}} + \Delta\mu_{\text{Cu}} + \Delta\mu_{\text{Se}} + \Delta\mu_{\text{O}} = \Delta H_f^{\text{BiCuSeO}}$, where $\Delta H_f^{\text{BiCuSeO}}$ is the formation enthalpy of BiCuSeO. Also, $\Delta\mu_{\text{Bi}}$, $\Delta\mu_{\text{Cu}}$, $\Delta\mu_{\text{O}}$, and $\Delta\mu_{\text{Se}}$ values should be such that other competing phases are unstable relative to BiCuSeO. In experiments, $\Delta\mu_i = 0$ corresponds to *i*-rich growth conditions and a large negative value of $\Delta\mu_i$ represents *i*-poor growth conditions.

Corrections to the defect formation energy arising from finite-size effects were included in E_{corr} , following the methodology of Lany and Zunger.^{52,62} The finite-size corrections include: (i) alignment of the average electrostatic potential between the neutral, defect-free host supercell and the charged, defect supercells, (ii) removal of artificial, long-range interactions between the image charges in periodic supercells that are charged, and (iii)

correction for Moss-Burnstein-type band filling⁶³ due to shallow defects.

The pylada-defects software⁶⁴ was used in this work for automating the point defect calculations, including the creation of defect supercells and calculation of finite-size corrections. The formation energies of native point defects (vacancy, anti-site, interstitial) and dopants (substitutional, interstitial) were calculated in charge states $q = -3, -2, -1, 0, +1, +2$, and $+3$. Additional charge states were considered where necessary. The plausible sites that can accommodate interstitial defects were determined by a Voronoi tessellation scheme implemented in pylada-defects.⁶⁴ The lowest-energy interstitial site was determined from the total energy of the interstitial configurations in the neutral charge state. The structures of Cu_i^{1+} and O_i^0 are shown in Figure S1. The optimized defect structures are available in a public repository.⁶⁵

2.4 Charge Carrier Concentrations

The free charge carrier concentrations were calculated by solving for the equilibrium Fermi energy (E_F^{eq}) satisfying the charge neutrality condition, which is expressed as

$$\sum_{D^q} \left[q N_D e^{-\Delta E_{D^q}/k_B T} \right] + p - n = 0 \quad (3)$$

where the sum runs over all defects D^q , N_D is the site concentration where defect D can be formed, k_B is the Boltzmann constant, T is the temperature, and p and n are the hole and electron concentrations, respectively. We assume that the defects formed at the synthesis temperature are kinetically “frozen in”; that is, when a material is quenched to lower temperatures, the defect concentrations reflect the defect thermodynamics at the synthesis temperature. Therefore, in Eq. 3, we use the synthesis temperature (not to be confused with the transport measurement temperature) to compute the net free carrier concentration. This commonly used assumption, emanating from the fact that most defects are not mobile at lower temperatures, provides accurate predictions of free carrier concentrations in agreement with experiments.^{45,46,66} The free carrier concentrations p and n are calculated as

$$p = \int_{-\infty}^{\text{VBM}} g(E) [1 - f(E)] dE \quad (4)$$

$$n = \int_{\text{CBM}}^{\infty} g(E) f(E) dE$$

where $f(E)$ is the Fermi-Dirac distribution. The density of states $g(E)$ was calculated using DFT with a Γ -centered $12 \times 12 \times 6$ k -point grid⁶⁷ and the tetrahedron method for Brillouin zone integration (Section 2.2).

3 Results and Discussion

3.1 Native Point Defects in BiCuSeO

Our convex hull analysis suggests that there are 12 distinct four-phase stability regions of BiCuSeO in the quaternary equilibrium Bi-Cu-Se-O phase space. Each stability region is defined by the equilibrium between BiCuSeO and three other competing phases.

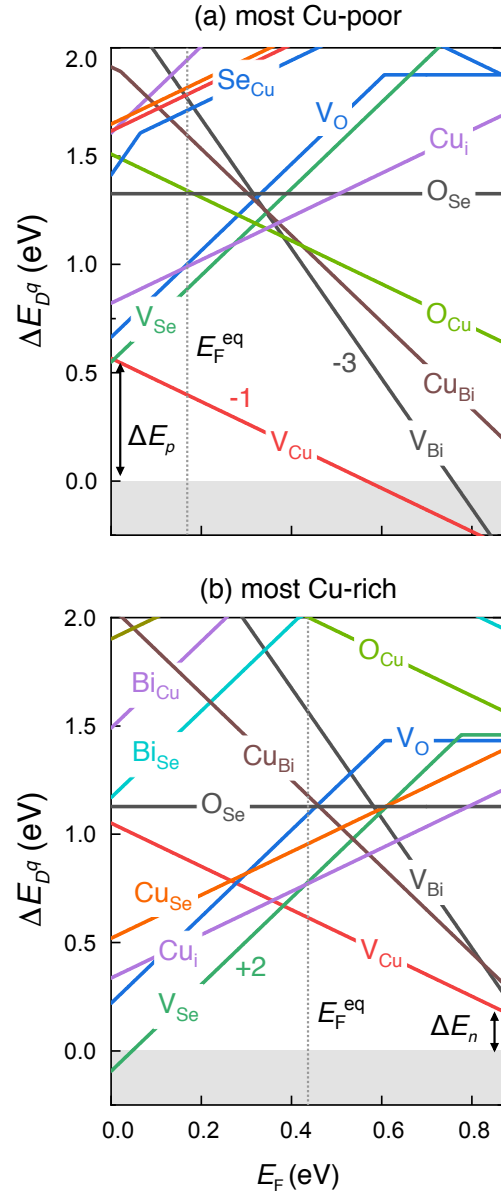


Fig. 2 Formation energies of native defects in BiCuSeO are shown for the (a) most Cu-poor growth condition (equilibrium with Se, Bi_2O_3 , and $\text{Bi}_2\text{O}_2\text{Se}$) with the highest free hole concentration of $1.3 \times 10^{20} \text{ cm}^{-3}$, and (b) most Cu-rich conditions (equilibrium with Bi, Cu_2O , and Cu_2Se) with lowest free hole concentration of $5.1 \times 10^{18} \text{ cm}^{-3}$, assuming a synthesis temperature of 973 K. The equilibrium Fermi energy is marked by the dotted vertical lines. Under Cu-poor conditions, BiCuSeO is natively a degenerate p -type semiconductor with scope for higher hole doping because of the large p -type dopability window (ΔE_p). Under the most Cu-rich condition, BiCuSeO has an n -type dopability window (ΔE_n) suggesting the possibility of n -type doping. The formation energies of all native defects are shown in Figure S3 in the supplementary information.

In the chemical potential space, these phase stability regions (Table S3) correspond to different elemental chemical potentials (μ_i in Eq. 2) and, as a result, different defect and carrier concentrations. In principle, the elemental chemical potentials can be controlled by modifying the growth conditions (e.g., Cu-poor vs. Cu-rich) and by performing phase boundary mapping,^{66,68} in which

the competing (impurity) phases of a material are explicitly determined to gauge the thermodynamic state of the material. We find that BiCuSeO is in thermodynamic equilibrium with Se, Bi₂O₃ and Bi₂O₂Se under the most Cu-poor growth condition, and in equilibrium with Bi, Cu₂O, and Cu₂Se under the most Cu-rich condition (Table S3).

Our defect calculations show that BiCuSeO is natively a *p*-type semiconductor under Cu-poor and Cu-rich growth conditions due to the low formation energy of the acceptor-like Cu vacancy (V_{Cu}), as shown in Figure 2. The relevant defects are those with the lowest formation energy at the equilibrium Fermi energy (E_F^{eq}), which is determined self-consistently by solving the charge neutrality condition (Section 2.4). In Figure 2, E_F^{eq} (marked with a dotted vertical line) is calculated assuming the typical synthesis temperature of 973 K. It has been shown experimentally that decreasing the Cu content in BiCu_{1-x}SeO increases the hole carrier concentration.⁶⁹ This can be explained by the low formation energy of the acceptor defect V_{Cu} under Cu-poor growth conditions, which is consistent with our predictions. Therefore, our results show that synthesizing BiCuSeO under Cu-poor growth conditions is a practical method to tune the hole carrier concentration due to the low formation energies of V_{Cu} .

The free hole concentration is maximized when BiCuSeO is grown under Cu-poor conditions (Figure 2a). Under the most Cu-rich conditions, the hole concentration is minimized (Figure 2b) due to charge compensation by electrons generated by the formation of Se vacancies (V_{Se}) and Cu interstitials (Cu_i). In contrast, hole compensation does not occur under Cu-poor conditions due to the higher formation energies of V_{Se} and Cu_i . Our predicted free hole concentrations in native BiCuSeO range from $5.1 \times 10^{18} \text{ cm}^{-3}$ (Cu-rich) to $1.3 \times 10^{20} \text{ cm}^{-3}$ (Cu-poor), in agreement with experimental measurements as shown in Figure 3.

A material is considered *p*-type dopable if the formation energy of the lowest-energy native donor defect is positive for all values of E_F within the band gap. In such a case, holes generated by a sufficiently soluble acceptor dopant are not compensated significantly by the electrons created by the native donor defect. Accordingly, a *p*-type dopability window (ΔE_p) may be defined at the VBM (Figure 2a), where a large positive ΔE_p indicates a highly *p*-type dopable material while a negative window would suggest difficulty in *p*-type doping. Similarly, an *n*-type dopability window (ΔE_n) is set by the formation energy of the lowest-energy native acceptor defect at the CBM and provides a measure of the potential for *n*-type doping. Under the most Cu-poor condition (Figure 2a), ΔE_p is $> 0.5 \text{ eV}$. In fact, we find BiCuSeO has a positive ΔE_p in 10 out of the 12 phase stability regions, which is not surprising considering the widespread success in *p*-type doping of BiCuSeO e.g., with group-2 alkaline-earth elements.^{4,10-13,71-73,76}

Perhaps the less anticipated result of our defect calculations is the prospect of doping BiCuSeO *n*-type, as evidenced by a positive ΔE_n under Cu-rich growth conditions (Figure 2b) where the formation of the electron-compensating acceptor V_{Cu} is most suppressed. As such, it may be possible to realize *n*-type doping of BiCuSeO provided a sufficiently soluble dopant can be found. In the following section, we discuss 23 different *p*- and *n*-type candidate dopants and the necessary growth conditions to maximize

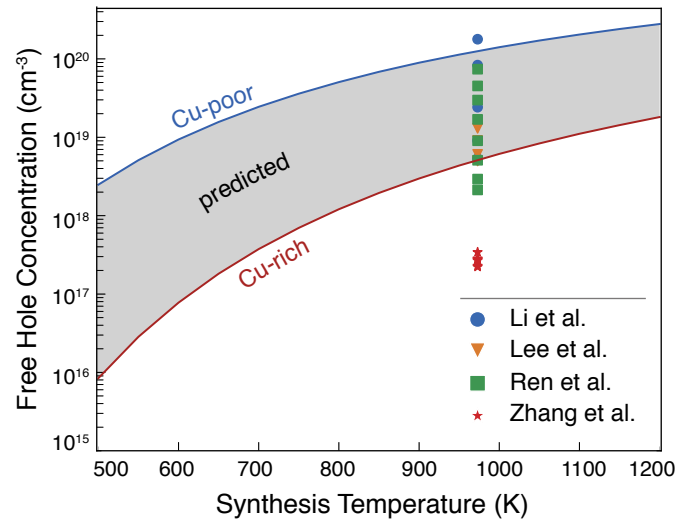


Fig. 3 Shaded area is the predicted range of free hole carrier concentrations in native BiCuSeO as a function of synthesis temperature. The highest (lowest) free hole concentrations are achieved under the most Cu-poor (Cu-rich) growth conditions. Experimentally measured hole carrier concentrations are shown as colored symbols (Li et al.,³ Lee et al.,¹⁷ Ren et al.,⁷⁰ Zhang et al.³¹). The predicted range of hole concentrations are in fair agreement with experiments.

the corresponding free carrier concentrations.

3.2 Dopants in BiCuSeO

We calculate the formation energies of 23 plausible *p*- and *n*-type dopants for BiCuSeO and the resulting free carrier concentrations generated by each dopant. All dopants are considered as substitutional defects, and some are additionally considered as interstitials where appropriate (e.g., Li). We calculate the carrier concentrations in all five-phase equilibrium regions where BiCuSeO is stable in the quinary Bi-Cu-Se-O-dopant phase space. The equilibrium phases and the corresponding free carrier concentrations in each phase region are listed in Tables S4 - S26. For each of the 23 dopants, the range of achievable free carrier concentrations are shown in Figure 4 and compared to available data from experimental doping studies.

Ideally, a dopant will extend the achievable range of carrier concentrations beyond what is attained through native self-doping. However, there are several factors that may limit the efficiency of a dopant. First, the solubility of a dopant is the critical limiting factor; if the formation energy of the substitutional (or interstitial) dopant is high compared to the native defects i.e., solubility of the dopant is low, then the concentration of free carriers generated by the dopant is insignificant compared to the native self-doped carrier concentration. Second, free carriers generated by the dopant may be charge compensated by the carriers of the opposite type (electrons, holes) generated by the native defects (donors, acceptors). Such a scenario occurs when the formation energy of the compensating native defect is low and is one of the central reasons why a dopability window (e.g., ΔE_p and ΔE_n in Figure 2) is necessary (but not sufficient) to realize the desired doping. Finally, certain dopants may form both substitutional (or

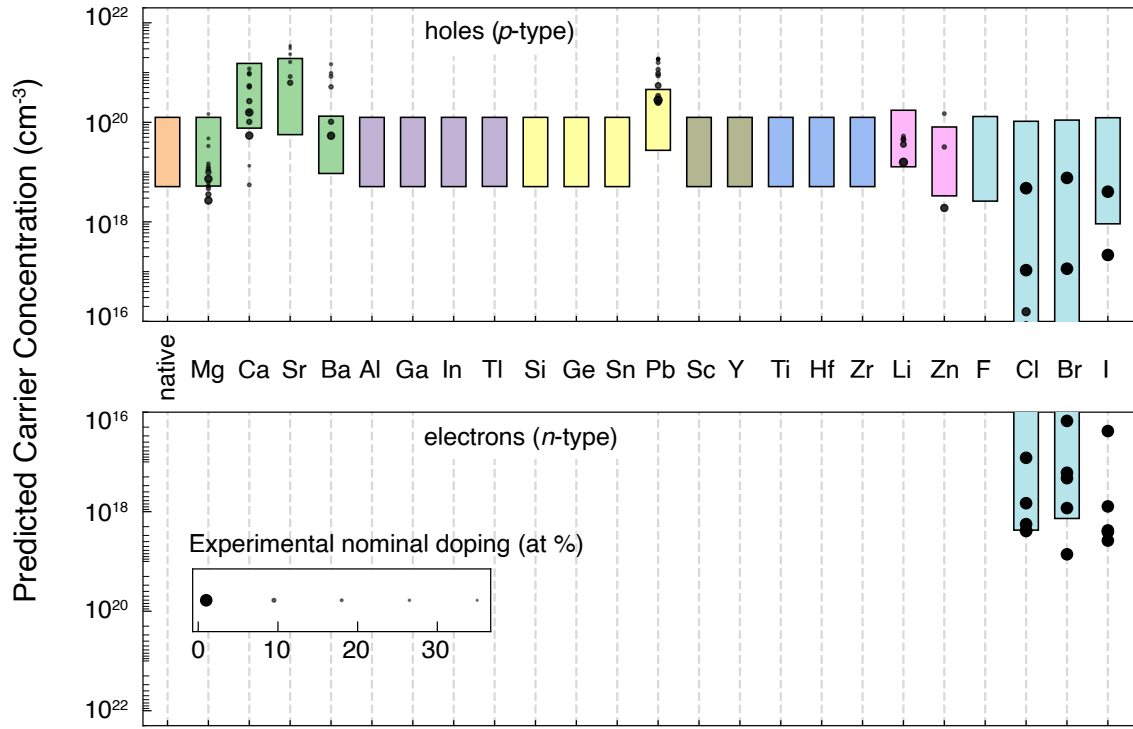


Fig. 4 Predicted range of free carrier concentrations for native defects and 23 dopants in BiCuSeO. The typical synthesis temperature of 973 K is used to calculate the carrier concentrations. The free hole (p -type) and electron (n -type) concentrations are shown in the top and bottom panels, respectively. Experimentally measured carrier concentrations are shown with solid black circles, ^{4,10–12,28,29,31,70–75} where the size of the marker corresponds to the nominal doping concentration ranging from 1 to 35 atomic %, as shown in the inset. Larger circles correspond to lower doping concentrations, whereas smaller circles to higher doping concentrations.

interstitial) acceptor and donor defects depending on the substituting site in the structure, such that the dopant generated electrons and holes self-compensate.

We find that the primary factor limiting n -type doping of BiCuSeO, despite being n -type dopable under Cu-rich growth conditions, is the low solubility of dopants, as discussed in detail in Section 3.2.2. Many of the dopants considered in this study exhibit high formation energies in BiCuSeO, even under the most dopant-rich thermodynamic conditions.

3.2.1 p -type Dopants

For the purposes of benchmarking our dopant calculations, we first consider a series of well-known p -type dopants in BiCuSeO, the group-2 alkaline-earth metals (Mg,^{71,72} Ca,^{4,12,73} Sr,^{10,76} and Ba^{11,13}). The formation energies of these dopants as substitutional defects on the Bi and Cu sites are shown in Figure S4. We find that the alkaline-earth metals preferentially substitute on the Bi site rather than the Cu site to form shallow acceptor-like defects, which is consistent with experimental observations of p -type doping with these group-2 elements. Preferential substitution on the Cu site would have resulted instead in donor-like substitutional defects and n -type doping.

It is well-known that Mg is the least effective p -type dopant in BiCuSeO out of the group-2 alkaline-earth metals.^{1,71,72} Our calculations suggest that this is due to the high formation energy of Mg_{Bi} relative to the dominant native acceptor defect V_{Cu} (Figure S4); in other words, the solubility of Mg in BiCuSeO is low. In contrast, Ca and Sr are highly effective with predicted maximum

free hole concentrations of $1.5 \times 10^{21} \text{ cm}^{-3}$ and $1.9 \times 10^{21} \text{ cm}^{-3}$ achieved under the most Ca- and Sr-rich doping conditions (Tables S5, S6). The predicted hole concentrations for Ca and Sr doping are also in good agreement with available experimental data (Figure 4).^{4,10,12,73} For low nominal doping (< 5 atomic %) with Ba, the measured hole concentrations are $\leq 10^{20} \text{ cm}^{-3}$, in agreement with our predicted range of 9.4×10^{18} – $1.3 \times 10^{20} \text{ cm}^{-3}$. This range of hole concentrations is comparable to native and Mg-doped BiCuSeO, suggesting that Ba is not an effective p -type dopant. The trend in the predicted hole concentrations for the group-2 dopants appear reasonable if we consider the ionic radii similarity between Bi^{3+} (0.96 Å) and the dopants (Mg: 0.72 Å, Ca: 1.00 Å, Sr: 1.18 Å, Ba: 1.35 Å).⁷⁷

However, there are reports of higher hole concentrations achieved in heavily Ba-doped BiCuSeO with 15 atomic % Ba.¹¹ The discrepancy between our predictions and experiments for high nominal doping concentrations could be due to the breakdown of the dilute doping assumption used in our defect calculations. In the dilute limit, it is assumed that the dopants introduce charge carriers (electrons or holes) without perturbing the electronic structure of the host material i.e., the rigid band approximation. Predictions of carrier concentrations based on the dilute doping assumption are in excellent agreement with experiments, as shown in this work for native BiCuSeO (Section 3.1) and in other studies on Mg_3Sb_2 ,⁶⁶ PbTe ,⁴⁵ KGaSb_4 ,⁴⁶ and CoSb_3 .⁷⁸ In Ref. 11, it is shown that 15 at. % Ba doping is associated with a concomitant ~ 1 % expansion in the lattice parameters, which

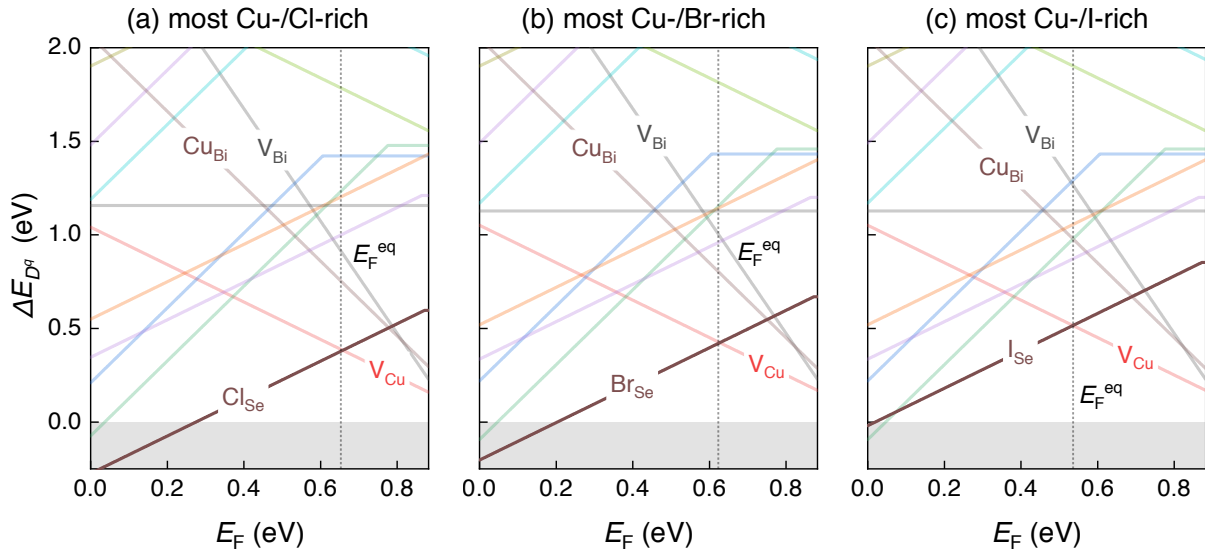


Fig. 5 Formation energy associated with (a) Cl, (b) Br, and (c) I doping in BiCuSeO. For each dopant, BiCuSeO is in thermodynamic equilibrium with the following impurity phases: (a) Bi, Cu₂Se, BiClO, and Bi₂₄Cl₁₀O₃₁, (b) Bi, Bi₄Br₂O₅, Cu₂O, and Cu₂Se, and (c) Bi, Cu₂Se, Cu₂O, and Bi₄I₂O₅. Halogens prefer to occupy the Se site (dopant substitutions on the O site are higher in energy and not shown). The native defects of BiCuSeO, from Figure 2, are shown in lighter color. The equilibrium Fermi energy (E_F^{eq}) determined by charge neutrality at 973 K are shown as vertical dotted lines.

clearly indicates that the dilute doping assumption may no longer valid. For such high doping concentrations, interactions between the dopant atoms become prevalent, which are not considered in the dilute doping model. Nonetheless, the predicted carrier concentration ranges of the other group-2 dopants (Mg, Ca, Sr) are in agreement with experiments, suggesting that the maximum carrier concentration attainable through group-2 doping has been already achieved in experiments. Further increases in hole concentrations for *p*-type BiCuSeO is unlikely to be achieved with group-2 doping.

3.2.2 *n*-type Dopants

Our calculated native defect formation energetics reveal that BiCuSeO is *n*-type dopable under Cu-rich growth conditions (Section 3.1). Combined with the fact that the *n*-type performance of BiCuSeO is predicted to surpass that of *p*-type (Section 1), it is worthwhile to search for efficient *n*-type dopants. In our search for *n*-type dopants, we assess 19 different elements, including those in group-1 (Li), group-3 (Sc, Y), group-4 (Ti, Zr, Hf), group-12 (Zn), group-13 (Al, Ga, In, Tl) group-14 (Si, Ge, Sn, Pb), and group-17 (F, Cl, Br, I).

Through this broad search, we find that only group-17 halogens (Cl, Br) serve as *n*-type dopants in BiCuSeO (Figure 4). The formation energies of the substitutional halogen dopants in BiCuSeO under the most halogen-rich thermodynamic conditions (to maximize solubility) are shown in Figure 5. The highest achievable free electron concentration by Cl doping is predicted to be $2.4 \times 10^{18} \text{ cm}^{-3}$, when BiCuSeO is in equilibrium with Bi, Cu₂Se, BiClO, and Bi₂₄Cl₁₀O₃₁ (Table S24). Similarly, Br is predicted to be an *n*-type dopant with highest electron concentration of $1.4 \times 10^{18} \text{ cm}^{-3}$ when in equilibrium with Bi, Bi₄Br₂O₅, Cu₂O, and Cu₂Se (Table S25). In contrast, we find that F and I are ineffective *n*-type halogen dopants (Figure 5c, Figure S5).

Zhang et al. reported *n*-type BiCuSeO by doping the material with Cl, Br, and I,^{30,31} providing valuable experimental evidence that BiCuSeO can indeed be doped *n*-type. Our finding that BiCuSeO is *n*-type dopable (Section 3.1) is retrospectively corroborated by these experiments. The same experimental studies^{30,31} report that halogen doping induces an anomalous *p-n-p* transition in the conductivity type with increasing temperature, which the authors attribute to weak, thermally unstable Cu-X ($X = \text{Cl, Br, I}$) bonds compared to the Cu-Se bond strength in the parent material.³¹ Based on our results, we suggest that the different thermodynamic states of the quinary Bi-Cu-Se-O-X ($X = \text{Cl, Br, I}$) phase space be explored in detail e.g., through phase boundary mapping^{66,79,80} to understand the observed *p-n-p* transition in the conductivity type. In phase boundary mapping, the presence of specific dopant-related competing phases in a sample is the signature of the corresponding thermodynamic state defined by the elemental chemical potentials e.g., Cu-/Cl-rich. The solubility of dopants in these different thermodynamic states play a crucial role in the resulting carrier concentration, as demonstrated in several studies.^{68,81} Moreover, studies on the thermal stability of BiCuSeO have suggested that the material is prone to Se volatilization especially at higher temperatures,^{82,83} which likely affects the dopant solubility given that our results predict the substitution of the halogen atoms on the Se site. In light of our results which indicate that both *n*- and *p*-type conductivity (Figure 3) are possible with Cl and Br depending on the thermodynamic state, we suggest that the anomalous *p-n-p* transition be revisited with further experimental analysis.

In contrast to experiments, we predict that I is not an *n*-type dopant in BiCuSeO (Figure 4) due to its low solubility compared to Cl and Br. It is curious that although our calculated carrier concentrations of *p*-type dopants (e.g., Ca, Sr) match experimental values rather well especially at low nominal doping concen-

trations, I is the only dopant for which our predictions do not agree with experiments. This is especially surprising since the nominal concentration of I in experiments is 1 at. %, ³¹ which is much lower than the nominal doping concentrations of the other dopants. Due to the limited number of halogen doping studies, it is difficult to gauge the exact cause of the disagreement. As mentioned before, the apparent *p-n-p* transition in the conductivity type with temperature ^{30,31} suggests some anomalous behavior of the material. Further experimental studies of halogen doping in conjunction with first-principles defect and dopant calculations are needed to resolve these issues.

Apart from the halogens, we find that none of the other considered *n*-type dopants are effective. While Li and Zn are known *p*-type dopants in BiCuSeO, ^{28,74,84} we wanted to explore the possibility of *n*-type doping if donor defects, Li_i and Zn_{Cu} , are favorable under certain thermodynamic equilibrium conditions. However, our results suggest that this is not the case for Li and Zn doping. For example, Li preferentially substitutes on the Bi site (Li_{Bi}) to form an acceptor defect that leads to *p*-type rather than the desired *n*-type doping (Figure S6). As expected, Li isovalently substitutes the Cu site forming the neutral Li_{Cu} defect. Our predicted range of carrier concentrations for Li-doped BiCuSeO matches the experimentally-measured hole concentrations ⁷⁴ (Figure 4), suggesting that the formation of Li_i is not favorable. For Zn, we predict that the substitution on the Cu site (Zn_{Cu} in Figure S7) is associated with a high formation energy such that the BiCuSeO is still *p*-type with free hole concentration of $3.3 \times 10^{18} \text{ cm}^{-3}$ (Table S9).

Group-3 (Sc, Y) and group-13 (Al, Ga, and In) elements are found to be isovalent dopants preferentially substituting on the Bi site (Figures S8, S10). Substitution on the Cu site, which creates donor defects, is associated with high formation energies. It is interesting that Tl, which is also a group-13 element, acts as an acceptor on the Bi site instead of an isovalent dopant (Figure S10d). However, the high formation energies i.e., low solubility of group-3 and group-13 dopants in BiCuSeO make them ineffective *n*-type dopants (Figure 4). We also find that group-4 dopants (Ti, Zr, Hf) are also ineffective due to their low solubility even under the most dopant-rich and Cu-rich conditions (Figure S9). Therefore, these dopants do not extend the range of achievable carrier concentration from what is already attained through native self-doping (Figure 4).

We also consider *n*-type doping of BiCuSeO with group-14 elements (Si, Ge, Sn, Pb). It is worth mentioning that a previous computational study of group-14 dopants by Shen et al. suggested that Si is an exceptional *n*-type dopant for BiCuSeO. ⁸⁵ While our results agree that Si_{Bi} is a donor defect and Ge_{Bi} , Sn_{Bi} , and Pb_{Bi} are acceptors (Figure S11), the formation energies of group-14 dopants in BiCuSeO are too high to increase the free electron concentration. We believe that this discrepancy is attributed to the phase stability information included in our calculation of the defect formation energy. While Shen et al. assume that group-14 doped BiCuSeO is in thermodynamic equilibrium with the dopant in its elemental form i.e., $\Delta\mu_{\text{dopant}} = 0 \text{ eV}$, our phase stability analysis, which considers all possible competing phases (Tables S14 - S17), shows that this is not possible. For all

group-14 dopants, the most dopant-rich condition corresponds to $\Delta\mu_{\text{dopant}} < 0 \text{ eV}$. For example, we find Si-doped BiCuSeO is in equilibrium with elemental Bi, Cu_3Se_2 , Bi_2Se_3 , and SiO_2 in the most Si-rich phase region (Table S14). As a result, our calculated formation energies of the group-14 dopants in BiCuSeO are higher than those calculated by Shen et al., ⁸⁵ suggesting that the solubility of group-14 dopants is much lower than previously predicted.

4 Conclusions and Outlook

We use first-principles defect calculations to show that the low formation energy of copper vacancies is responsible for the native *p*-type character of BiCuSeO. Interestingly, we find that BiCuSeO is also *n*-type dopable under Cu-rich growth conditions. Through a broad computational survey of plausible *n*-type dopants, we identify Cl and Br as the most effective *n*-type dopants. We find that more than half of the plausible dopants are ineffective, providing useful guidance for future experimental doping efforts; for *n*-type doping, experiments should continue to focus on halogen doping to resolve the anomalous temperature-dependent *p-n-p* transition.

BiCuSeO is a well-known *p*-type TE material. The prospects of *n*-type doping, as revealed by our defect calculations and recent experimental doping studies, prompt us to ask whether the electron concentration in BiCuSeO can be optimized to unlock the high *n*-type TE performance predicted by computations. Furthermore, it is also worth asking whether we can design chemical analogues of BiCuSeO, with similar thermopower and thermal conductivity, that can be doped both *p*- and *n*-type.

We may envision such a design possibility by comparing the defect energetics of BiCuSeO with one of its chemical analogues, LaCuSeO, which crystallizes in the same *P4/nmm* layered structure. While the formation energy of the acceptor V_{Cu} is relatively low in both compounds, which is expected due to the common $(\text{Cu}_2\text{Se}_2)^{2-}$ layers in both structures, there is little opportunity for *n*-type doping of LaCuSeO. ⁸⁶ The distinctly different *n*-type dopability of BiCuSeO and LaCuSeO can be explained by the relative positions of the conduction band edge (CBE). Heuristic guidelines suggest that compounds with lower CBEs tend to be *n*-type dopable. ^{87,88} Since the CBE of BiCuSeO, which is primarily derived from Bi-6*p* states, is lower than that of LaCuSeO, where the CBE is composed of Cu-4*s*/La-5*d* states, ⁴⁹ it is expected that LaCuSeO would be less *n*-type dopable compared to BiCuSeO. This heuristic comparison between LaCuSeO and BiCuSeO contextualizes chemical substitution as an inverse design principle to realize *p*- and *n*-type dopable materials. ^{48,89} By substituting Bi with an element with larger electron affinity e.g., Sb, that lowers the energy of the CBE, an *n*-type dopable analogue of BiCuSeO may be possible. The discovery and design of such chemical analogues will be the focus of a future study.

Acknowledgements

MYT is funded by the United States Department of Energy through the Computational Science Graduate Fellowship (DOE CSGF) under grant number DE-SC0020347. JQ is funded by the NSF DIGI-MAT program, grant number 1922758. GJS acknowledges support from NSF DMR, DMREF grant number

1729487 and P.G. acknowledges support from NSF through award DMR-2102409. The research was performed using computational resources sponsored by the Department of Energy's Office of Energy Efficiency and Renewable Energy and located at the NREL. This research was also supported in part through the computational resources and staff contributions provided for the Quest high performance computing facility at Northwestern University, which is jointly supported by the Office of the Provost, the Office for Research, and Northwestern University Information Technology.

References

- 1 L.-D. Zhao, J. He, D. Berardan, Y. Lin, J.-F. Li, C.-W. Nan and N. Dragoe, *Energy Environ. Sci.*, 2014, **7**, 2900.
- 2 Y. Liu, L.-D. Zhao, Y. Zhu, Y. Liu, F. Li, M. Yu, D.-B. Liu, W. Xu, Y.-H. Lin and C.-W. Nan, *Adv. Energy Mater.*, 2016, **6**, 1502423.
- 3 F. Li, J.-F. Li, L.-D. Zhao, K. Xiang, Y. Liu, B.-P. Zhang, Y.-H. Lin, C.-W. Nan and H.-M. Zhu, *Energy Environ. Sci.*, 2012, **5**, 7188.
- 4 Y.-L. Pei, J. He, J.-F. Li, F. Li, Q. Liu, W. Pan, C. Barreateau, D. Berardan, N. Dragoe and L.-D. Zhao, *NPG Asia Mater.*, 2013, **5**, e47.
- 5 H. Shao, X. Tan, G.-Q. Liu, J. Jiang and H. Jiang, *Sci. Rep.*, 2016, **6**, 1.
- 6 X. Zhang, C. Chang, Y. Zhou and L.-D. Zhao, *Materials*, 2017, **10**, 198.
- 7 R. Liu, X. Tan, Y.-C. Liu, G.-K. Ren, J.-L. Lan, Z.-F. Zhou, C.-W. Nan and Y.-H. Lin, *Rare Metals*, 2018, **37**, 259.
- 8 G.-K. Ren, J.-L. Lan, L.-D. Zhao, C. Liu, H. Yuan, Y. Shi, Z. Zhou and Y.-H. Lin, *Mater. Today*, 2019, **29**, 68.
- 9 G. J. Snyder and E. S. Toberer, *Nat. Mater.*, 2008, **7**, 105.
- 10 C. Barreateau, D. Berardan, E. Amzallag, L. Zhao and N. Dragoe, *Chem. Mater.*, 2012, **24**, 3168.
- 11 J. Li, J. Sui, Y. Pei, C. Barreateau, D. Berardan, N. Dragoe, W. Cai, J. He and L.-D. Zhao, *Energy Environ. Sci.*, 2012, **5**, 8543.
- 12 F. Li, T.-R. Wei, F. Kang and J.-F. Li, *J. Mater. Chem. A*, 2013, **1**, 11942.
- 13 J. Sui, J. Li, J. He, Y.-L. Pei, D. Berardan, H. Wu, N. Dragoe, W. Cai and L.-D. Zhao, *Energy Environ. Sci.*, 2013, **6**, 2916.
- 14 J. Li, J. Sui, Y. Pei, X. Meng, D. Berardan, N. Dragoe, W. Cai and L.-D. Zhao, *J. Mater. Chem. A*, 2014, **2**, 4903.
- 15 M. Zhang, J. Yang, Q. Jiang, L. Fu, Y. Xiao, Y. Luo, D. Zhang, Y. Cheng and Z. Zhou, *J. Electron. Mater.*, 2015, **44**, 2849.
- 16 J.-L. Lan, C. Deng, W. Ma, G.-K. Ren, Y.-H. Lin and X. Yang, *J. Alloy Compd.*, 2017, **708**, 955.
- 17 D. Sun Lee, T.-H. An, M. Jeong, H.-S. Choi, Y. Soo Lim, W.-S. Seo, C.-H. Park, C. Park and H.-H. Park, *Appl. Phys. Lett.*, 2013, **103**, 232110.
- 18 J.-L. Lan, W. Ma, C. Deng, G.-K. Ren, Y.-H. Lin and X. Yang, *J. Mater. Sci.*, 2017, **52**, 11569.
- 19 A. Achour, K. Chen, M. J. Reece and Z. Huang, *J. Alloy Compd.*, 2018, **735**, 861.
- 20 Y. Liu, J. Ding, B. Xu, J. Lan, Y. Zheng, B. Zhan, B. Zhang, Y. Lin and C. Nan, *Appl. Phys. Lett.*, 2015, **106**, 233903.
- 21 S. Tan, H. Lei, D. Shao, H. Lv, W. Lu, Y. Huang, Y. Liu, B. Yuan, L. Zu, X. Kan, W. Song and Y. Sun, *Appl. Phys. Lett.*, 2014, **105**, 082109.
- 22 Y.-C. Liu, Y.-H. Zheng, B. Zhan, K. Chen, S. Butt, B. Zhang and Y.-H. Lin, *J. Eur. Ceram. Soc.*, 2015, **35**, 845.
- 23 M. U. Farooq, S. Butt, K. Gao, X. L. Pang, X. Sun, Asfandiyar, F. Mohamed, A. Ahmad, A. Mahmood and N. Mahmood, *J. Alloy. Compd.*, 2017, **691**, 572.
- 24 J. Yan, P. Gorai, B. Ortiz, S. Miller, S. A. Barnett, T. Mason, V. Stevanović and E. S. Toberer, *Energy Environ. Sci.*, 2015, **8**, 983.
- 25 S. A. Miller, P. Gorai, B. R. Ortiz, A. Goyal, D. Gao, S. A. Barnett, T. O. Mason, G. J. Snyder, Q. Lv, V. Stevanović and E. S. Toberer, *Chem. Mater.*, 2017, **29**, 2494.
- 26 J. Yang, G. Yang, G. Zhang and Y. X. Wang, *J. Mater. Chem. A*, 2014, **2**, 13923.
- 27 R. McKinney, P. Gorai, E. S. Toberer and V. Stevanovic, *Chem. Mater.*, 2019, **31**, 2048.
- 28 G.-K. Ren, S. Butt, Y.-C. Liu, J.-L. Lan, Y.-H. Lin, C.-W. Nan, F. Fu and X.-F. Tang, *Phys. Status Solidi A*, 2014, **211**, 2616.
- 29 Z. Zhou, X. Tan, G. Ren, Y. Lin and C. Nan, *J. Electron. Mater.*, 2017, **46**, 2593.
- 30 X. Zhang, D. Feng, J. He and L.-D. Zhao, *J. Solid State Chem.*, 2018, **258**, 510.
- 31 X. Zhang, D. Wang, G. Wang and L.-D. Zhao, *Ceram. Int.*, 2019, **45**, 14953.
- 32 S. Tan, C. Gao, C. Wang, Y. Sun, Q. Jing, Q. Meng, T. Zhou and J. Ren, *Solid State Sci.*, 2019, **98**, 106019.
- 33 G. Kresse and J. Furthmüller, *Comp. Mater. Sci.*, 1996, **6**, 15.
- 34 G. Kresse and J. Furthmüller, *Phys. Rev. B*, 1996, **54**, 11169.
- 35 P. E. Blöchl, *Phys. Rev. B*, 1994, **50**, 17953.
- 36 G. Kresse and D. Joubert, *Phys. Rev. B*, 1999, **59**, 1758.
- 37 S. Dudarev, G. Botton, S. Savrasov, C. Humphreys and A. Sutton, *Phys. Rev. B*, 1998, **57**, 1505.
- 38 P. Gorai, E. S. Toberer and V. Stevanović, *Phys. Chem. Chem. Phys.*, 2016, **18**, 31777.
- 39 J. P. Perdew, K. Burke and M. Ernzerhof, *Phys. Rev. Lett.*, 1996, **77**, 3865.
- 40 P. Gorai, E. S. Toberer and V. Stevanović, *J. Mater. Chem. A*, 2016, **4**, 11110.
- 41 J. Klimeš, D. R. Bowler and A. Michaelides, *Phys. Rev. B*, 2011, **83**, 195131.
- 42 N. Marom, A. Tkatchenko, M. Scheffler and L. Kronik, *J. Chem. Theory Comput.*, 2010, **6**, 81.
- 43 P. E. Blöchl, O. Jepsen and O. K. Andersen, *Phys. Rev. B*, 1994, **49**, 16223.
- 44 H. Peng, D. O. Scanlon, V. Stevanovic, J. Vidal, G. W. Watson and S. Lany, *Phys. Rev. B*, 2013, **88**, 115201.
- 45 A. Goyal, P. Gorai, E. S. Toberer and V. Stevanović, *npj Comput. Mater.*, 2017, **3**, 1.

- 46 B. R. Ortiz, P. Gorai, V. Stevanovic and E. S. Toberer, *Chem. Mater.*, 2017, **29**, 4523.
- 47 P. Gorai, B. R. Ortiz, E. S. Toberer and V. Stevanović, *J. Mater. Chem. A*, 2018, **6**, 13806.
- 48 P. Gorai, A. Ganose, A. Faghaninia, A. Jain and V. Stevanović, *Mater. Horiz.*, 2020, **7**, 1809.
- 49 H. Hiramatsu, H. Yanagi, T. Kamiya, K. Ueda, M. Hirano and H. Hosono, *Chem. Mater.*, 2008, **20**, 326.
- 50 W. Setyawan and S. Curtarolo, *Comp. Mater. Sci.*, 2010, **49**, 299.
- 51 S. Curtarolo, W. Setyawan, G. L. Hart, M. Jahnatek, R. V. Chepulskii, R. H. Taylor, S. Wang, J. Xue, K. Yang, O. Levy, M. J. Mehl, H. T. Stokes, D. O. Demchenko and D. Morgan, *Comp. Mater. Sci.*, 2012, **58**, 218.
- 52 S. Lany and A. Zunger, *Model. Simul. Mater. Sc.*, 2009, **17**, 084002.
- 53 C. Freysoldt, B. Grabowski, T. Hickel, J. Neugebauer, G. Kresse, A. Janotti and C. G. Van de Walle, *Rev. Mod. Phys.*, 2014, **86**, 253.
- 54 S. Lany, *Phys. Rev. B*, 2008, **78**, 245207.
- 55 V. Stevanović, S. Lany, X. Zhang and A. Zunger, *Phys. Rev. B*, 2012, **85**, 115104.
- 56 D. D. Wagman, W. H. Evans, V. B. Parker, R. H. Schumm and I. Halow, 1982.
- 57 D. R. Lide, *CRC Handbook of Chemistry and Physics*, 1992.
- 58 A. Olin, 2005.
- 59 H. Oppermann, H. Göbel, P. Schmidt, H. Schadow and V. Vasiliev, *Z. Naturforsch. B*, 1999, **54**, 261.
- 60 G. Moiseev, N. Vatolin and N. Belousova, *J. Therm. Anal. Calorim.*, 2000, **61**, 289.
- 61 N. Babanly, Y. A. Yusibov, Z. Aliev and M. Babanly, *Russ. J. Inorg. Chem.*, 2010, **55**, 1471.
- 62 S. Lany and A. Zunger, *Phys. Rev. B*, 2008, **78**, 235104.
- 63 E. Burstein, *Phys. Rev.*, 1954, **93**, 632.
- 64 A. Goyal, P. Gorai, H. Peng, S. Lany and V. Stevanović, *Comp. Mater. Sci.*, 2017, **130**, 1.
- 65 <https://github.com/prashungorai/papers/tree/main/2021/BiCuSeO>.
- 66 S. Ohno, K. Imasato, S. Anand, H. Tamaki, S. D. Kang, P. Gorai, H. K. Sato, E. S. Toberer, T. Kanno and G. J. Snyder, *Joule*, 2018, **2**, 141.
- 67 H. J. Monkhorst and J. D. Pack, *Phys. Rev. B*, 1976, **13**, 5188.
- 68 M. Wood, M. Y. Toriyama, S. Dugar, J. Male, S. Anand, V. Stevanović and G. J. Snyder, *Adv. Energy Mater.*, 2021, **11**, 2100181.
- 69 Y. Liu, L.-D. Zhao, Y. Liu, J. Lan, W. Xu, F. Li, B.-P. Zhang, D. Berardan, N. Dragoe, Y.-H. Lin, C.-W. Nan, J.-F. Li and H. Zhu, *J. Am. Chem. Soc.*, 2011, **133**, 20112.
- 70 G.-K. Ren, S. Wang, Z. Zhou, X. Li, J. Yang, W. Zhang, Y.-H. Lin, J. Yang and C.-W. Nan, *Nat. Comm.*, 2019, **10**, 1.
- 71 J.-L. Lan, B. Zhan, Y.-C. Liu, B. Zheng, Y. Liu, Y.-H. Lin and C.-W. Nan, *Appl. Phys. Lett.*, 2013, **102**, 123905.
- 72 J. Li, J. Sui, C. Barreateau, D. Berardan, N. Dragoe, W. Cai, Y. Pei and L.-D. Zhao, *J. Alloy Compd.*, 2013, **551**, 649.
- 73 C.-L. Hsiao and X. Qi, *Acta Mater.*, 2016, **102**, 88.
- 74 J. Tang, R. Xu, J. Zhang, D. Li, W. Zhou, X. Li, Z. Wang, F. Xu, G. Tang and G. Chen, *ACS Appl. Mater. Int.*, 2019, **11**, 15543.
- 75 J.-L. Lan, Y.-C. Liu, B. Zhan, Y.-H. Lin, B. Zhang, X. Yuan, W. Zhang, W. Xu and C.-W. Nan, *Adv. Mater.*, 2013, **25**, 5086.
- 76 L.-D. Zhao, D. Berardan, Y.-L. Pei, C. Byl, L. Pinsard-Gaudart and N. Dragoe, *Appl. Phys. Lett.*, 2010, **97**, 092118.
- 77 R. D. Shannon, *Acta Crystall. A-Cryst.*, 1976, **32**, 751.
- 78 G. Li, U. Aydemir, M. Wood, W. A. Goddard III, P. Zhai, Q. Zhang and G. J. Snyder, *Chem. Mater.*, 2017, **29**, 3999.
- 79 C. M. Crawford, B. R. Ortiz, P. Gorai, V. Stevanovic and E. S. Toberer, *J. Mater. Chem. A*, 2018, **6**, 24175.
- 80 P. Jood, J. P. Male, S. Anand, Y. Matsushita, Y. Takagiwa, M. G. Kanatzidis, G. J. Snyder and M. Ohta, *J. Am. Chem. Soc.*, 2020, **142**, 15464.
- 81 R. Orenstein, J. P. Male, M. Toriyama, S. Anand and G. J. Snyder, *J. Mater. Chem. A*, 2021, **9**, 7208.
- 82 F. Li, T.-R. Wei, F. Kang and J.-F. Li, *J. Alloy Compd.*, 2014, **614**, 394.
- 83 A. Novitskii, G. Guélou, A. Voronin, T. Mori and V. Khovaylo, *Scripta Mater.*, 2020, **187**, 317.
- 84 G. Ren, S. Butt, C. Zeng, Y. Liu, B. Zhan, J. Lan, Y. Lin and C. Nan, *J. Electron. Mater.*, 2015, **44**, 1627.
- 85 J. Shen and Y. Chen, *ACS Appl. Mater. Inter.*, 2017, **9**, 27372.
- 86 D. O. Scanlon, J. Buckeridge, C. R. A. Catlow and G. W. Watson, *J. Mater. Chem. C*, 2014, **2**, 3429.
- 87 S. Zhang, S.-H. Wei and A. Zunger, *J. Appl. Phys.*, 1998, **83**, 3192.
- 88 S.-H. Wei, *Comp. Mater. Sci.*, 2004, **30**, 337.
- 89 J. Qu, V. Stevanović, E. Ertekin and P. Gorai, *J. Mater. Chem. A*, 2020, **8**, 25306.

— **Supplementary Information** —

Defect Chemistry and Doping of BiCuSeO

Michael Y. Toriyama,^{*,†} Jiaxing Qu,[‡] G. Jeffrey Snyder,[†] and Prashun Gorai^{*,¶}

[†]*Materials Science and Engineering, Northwestern University, Evanston, IL 60208, USA.*

[‡]*Mechanical Engineering, University of Illinois at Urbana-Champaign, Urbana, IL 61801.*

[¶]*Metallurgical and Materials Engineering, Colorado School of Mines, Golden, CO 80401, USA.*

E-mail: MichaelToriyama2024@u.northwestern.edu; pgorai@mines.edu

Pristine and Interstitial Structures

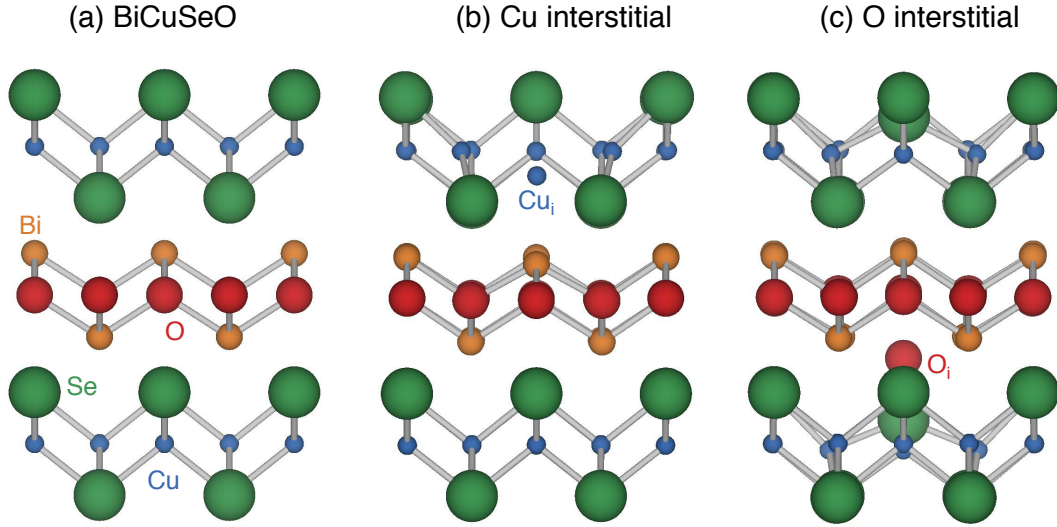


Figure S1: (a) Crystal structure of BiCuSeO, (b) Structure of copper interstitial (Cu_i^{+1}), and (c) Structure of oxygen interstitial (O_i^0).

Calculated Lattice Parameters

Method	a (Å)	c (Å)	a Error (%)	c Error (%)
PBE + U	3.949	9.062	0.52	1.49
vdW + U	3.926	8.927	0.08	0.02
Experiment ¹	3.929	8.929		

Table S1: Lattice constants calculated using different functionals and compared to experimental values.¹ The experimental lattice constants are better reproduced with the van der Waals-corrected functional with Hubbard U correction (vdW+ U).

Electronic Structure of BiCuSeO

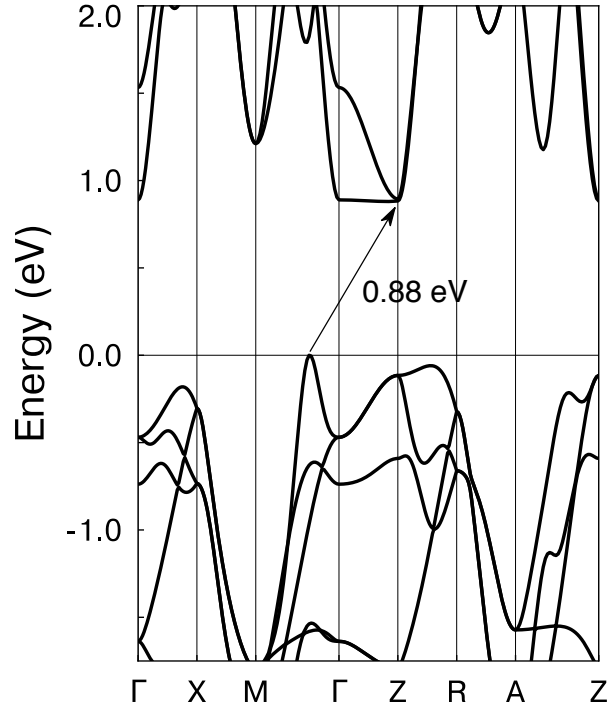


Figure S2: Computed electronic band structure of BiCuSeO along the special k -point paths of the Brillouin zone. The band edge positions are rigidly shifted to according to GW and spin-orbit coupling calculations.

Elemental Reference Chemical Potentials

Element	μ^0 (eV)
Bi	-4.42
Cu	-1.65
Se	-3.63
O	-4.76
Li	-1.64
Zn	-0.80
Mg	-1.00
Ca	-1.60
Sr	-1.15
Ba	-1.34
Al	-2.81
Ga	-2.30
In	-2.27
Tl	-2.35
Si	-4.74
Ge	-4.07
Sn	-3.65
Pb	-3.79
Sc	-4.49
Y	-4.81
Ti	-5.39
Zr	-5.97
Hf	-7.51
F	-1.52
Cl	-1.73
Br	-1.74
I	-1.67

Table S2: Elemental reference chemical potentials μ^0 , fitted to experimental formation enthalpies.^{2,3} GGA+U functional is used to calculate the total energy of the compounds used in the fitting.

Phase Equilibria of BiCuSeO

Equilibrium Phases	$\Delta\mu_{\text{Bi}}$	$\Delta\mu_{\text{Cu}}$	$\Delta\mu_{\text{O}}$	$\Delta\mu_{\text{Se}}$	$p - n \text{ (cm}^{-3}\text{)}$
Se, Cu_3Se_2 , Bi_2Se_3	-0.378	-0.62	-1.923	0.0	7.36×10^{19}
Se, $\text{Bi}_2\text{O}_2\text{Se}$, Bi_2O_3	-0.602	-0.708	-1.61	0.0	1.26×10^{20}
Se, $\text{Bi}_2\text{O}_2\text{Se}$, Bi_2Se_3	-0.378	-0.708	-1.835	0.0	1.25×10^{20}
Se, Cu_3Se_2 , Bi_2O_3	-0.865	-0.62	-1.435	0.0	7.48×10^{19}
Cu_2O , Cu_3Se_2 , Bi_2O_3	-0.603	-0.445	-1.61	-0.262	2.6×10^{19}
Cu_2Se , Cu_2O , Cu_3Se_2	-0.285	-0.318	-1.864	-0.453	1.13×10^{19}
Bi, Cu_2O , Bi_2O_3	0.0	-0.244	-2.012	-0.664	5.61×10^{18}
Bi, Cu_2Se , Cu_2O	0.0	-0.223	-2.054	-0.643	5.11×10^{18}
Bi, Cu_2Se , Cu_3Se_2	0.0	-0.318	-2.149	-0.453	1.1×10^{19}
Bi, Cu_3Se_2 , Bi_2Se_3	0.0	-0.452	-2.216	-0.252	2.33×10^{19}
Bi, $\text{Bi}_2\text{O}_2\text{Se}$, Bi_2O_3	0.0	-0.507	-2.012	-0.402	3.44×10^{19}
Bi, $\text{Bi}_2\text{O}_2\text{Se}$, Bi_2Se_3	0.0	-0.582	-2.087	-0.252	5.4×10^{19}

Table S3: Chemical potentials $\Delta\mu_i$ (in eV) in all phase regions of the quaternary Bi-Cu-Se-O phase space that are in equilibrium with BiCuSeO. The corresponding charge carrier concentration in each phase region, as determined by charge neutrality at the typical synthesis temperature of 973 K, is listed.

Native Defects in BiCuSeO

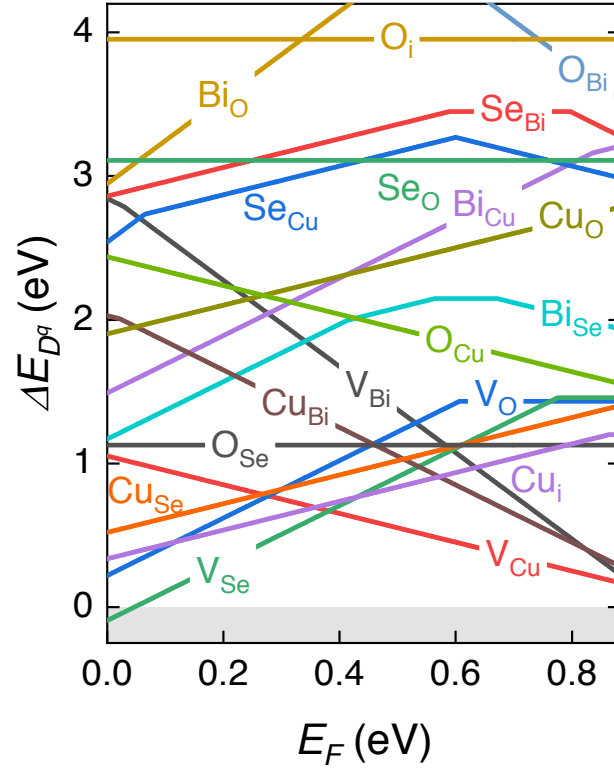


Figure S3: Formation energy (ΔE_{Dq}) as a function of Fermi energy (E_F) of all native defects in BiCuSeO under the most Cu-rich condition where BiCuSeO is in equilibrium with Bi, Cu_2Se , and Cu_2O .

Group-2 Doping: Mg, Ca, Sr, Ba

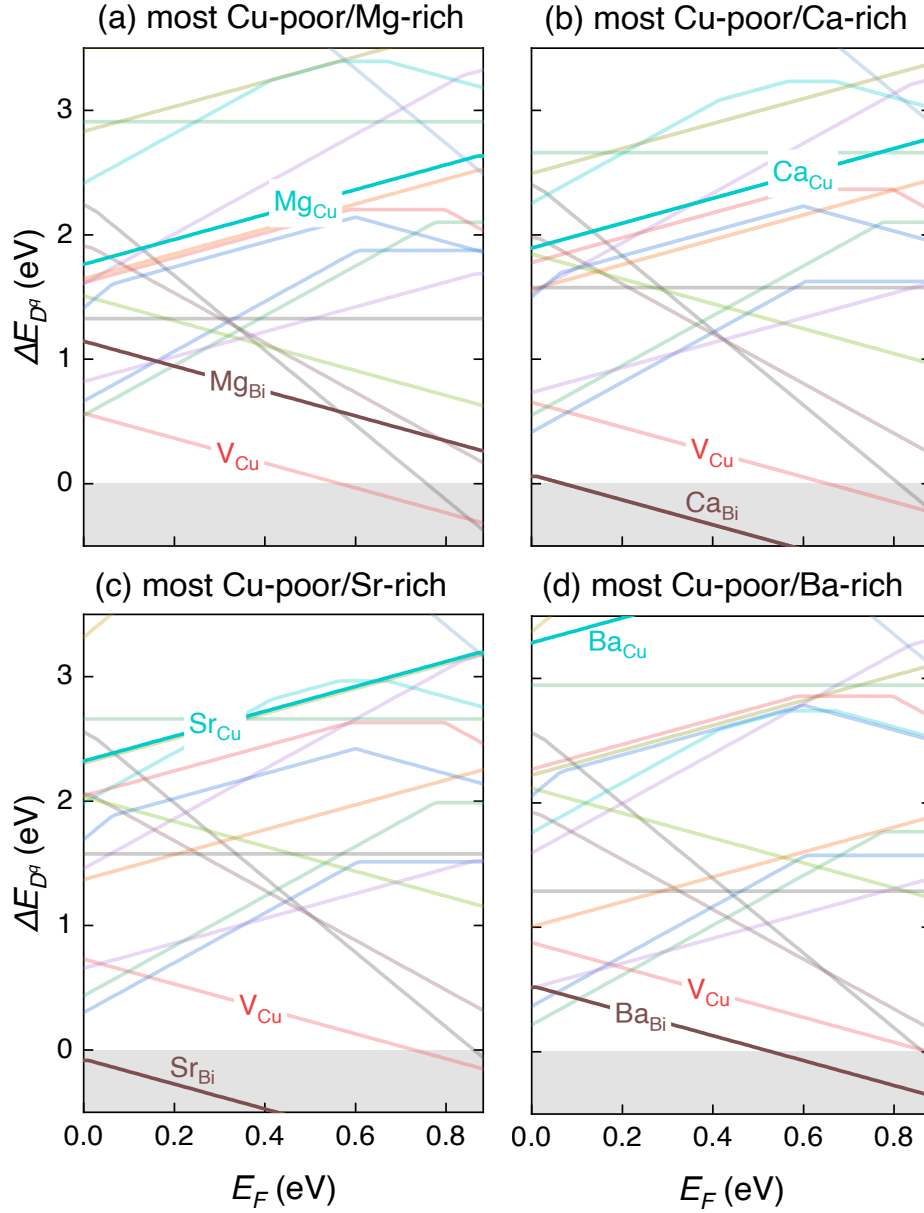


Figure S4: Formation energy of defects associated with (a) Mg, (b) Ca, (c) Sr, and (d) Ba doping under the most Cu-poor and dopant-rich conditions i.e., phase regions that yield the highest hole concentrations. BiCuSeO is in equilibrium with the following phases: (a) Se, MgO, Bi₂O₂Se, and Bi₂O₃, (b) Se, CaO, Cu₃Se₂, and CaSeO₃, (c) SrSeO₃, SrSe, Bi₂O₅Sr₂, and Cu₃Se₂, and (d) BaCu₂Se₂, BaSeO₃, Cu₃Se₂, and Ba₂Bi₄O₈. Native defects of BiCuSeO (Figure 2 in main text) are shown in lighter colors.

Group-17 Doping: F

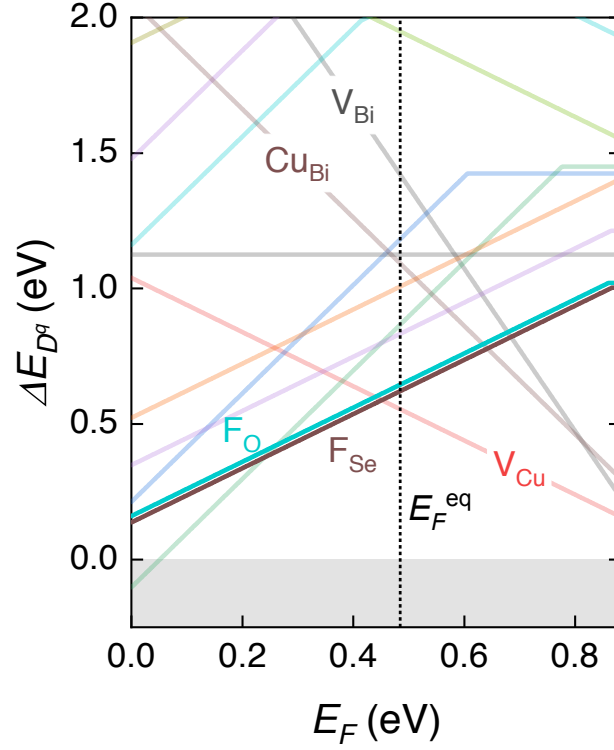


Figure S5: Formation energy of defects associated with F doping under the most Cu-rich condition, where BiCuSeO is in equilibrium with Bi, Cu₂O, Cu₂Se, and BiFO. Native defects of BiCuSeO (Figure 2 in main text) are shown in lighter colors. The equilibrium Fermi energy (E_F^{eq}), as determined by charge neutrality at 973 K, is marked with a dotted vertical line.

Group-1 Doping: Li

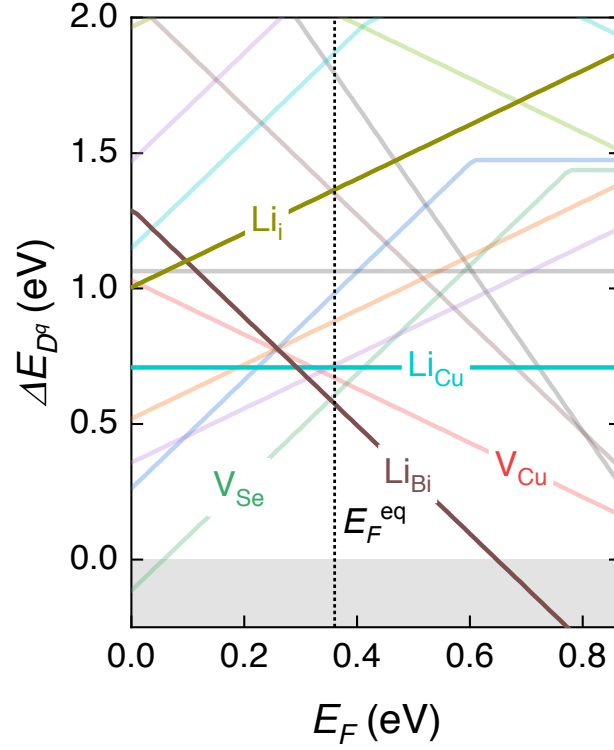


Figure S6: Formation energy of defects associated with Li doping in BiCuSeO under the most Cu-rich condition where BiCuSeO is in equilibrium with Bi, Cu_2O , Bi_2O_3 , and $\text{Cu}_8\text{Li}_8\text{O}_8$. Native defects of BiCuSeO (Figure 2 in main text) are shown in lighter colors. The equilibrium Fermi energy (E_F^{eq}), as determined by charge neutrality at 973 K, is marked with a dotted vertical line.

Group-12 Doping: Zn

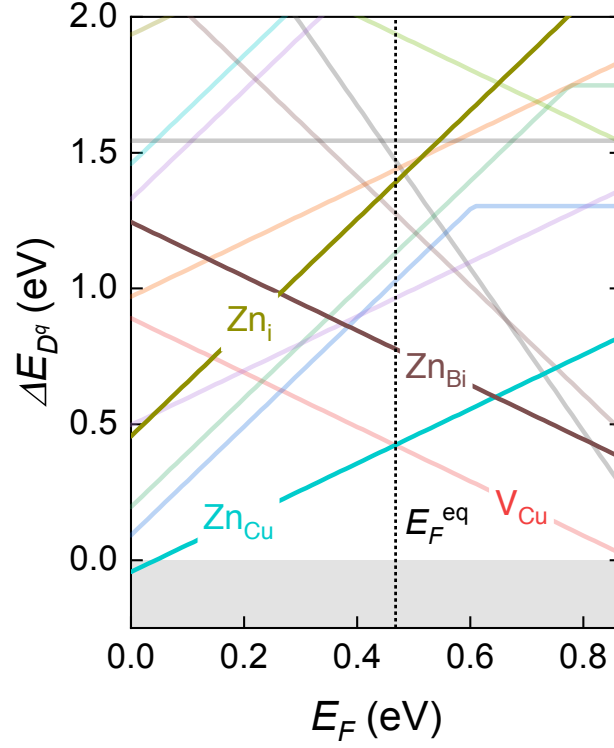


Figure S7: Formation energy of defects associated with Zn doping in BiCuSeO under the thermodynamic conditions where BiCuSeO is in equilibrium with Bi, Cu₃Se₂, ZnSe, and ZnO. Native defects of BiCuSeO (Figure 2 in main text) are shown in lighter colors. The equilibrium Fermi energy (E_F^{eq}), as determined by charge neutrality at 973 K, is marked with a dotted vertical line.

Group-3 Doping: Sc, Y

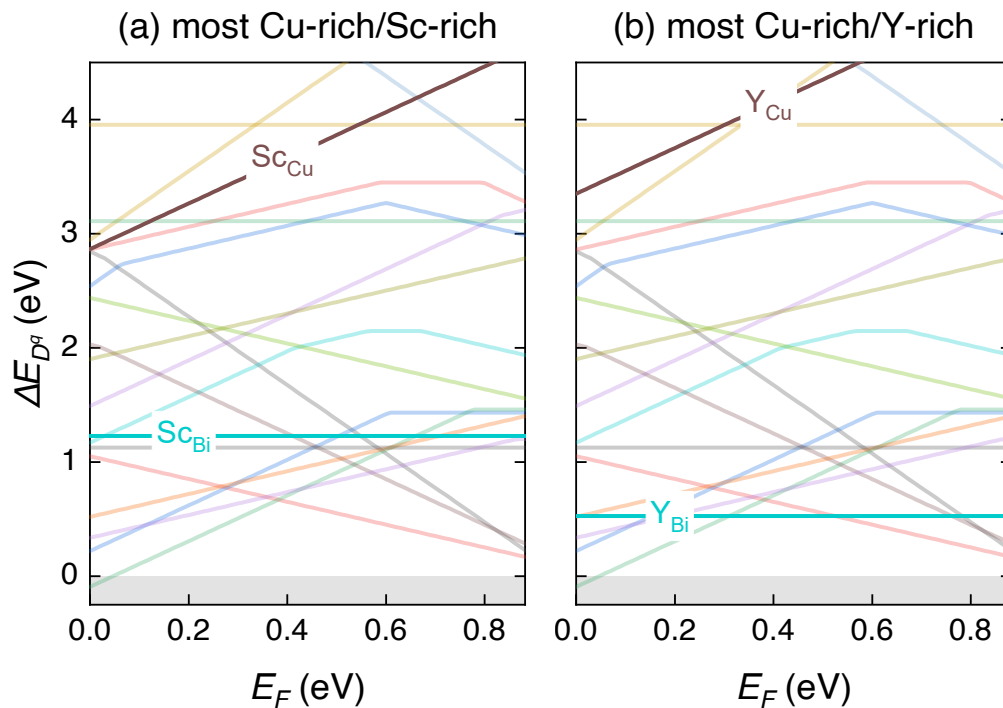


Figure S8: Formation energy of defects associated with (a) Sc, and (b) Y doping in BiCuSeO under the most Cu-rich conditions where BiCuSeO is in equilibrium with (a) Bi, Cu₂Se, Cu₂O, and CuO₂Sc, and (b) Bi, Cu₂Se, Cu₂O, and Y₂O₃. Native defects of BiCuSeO (Figure 2 in main text) are shown in lighter colors. The equilibrium Fermi energy (E_F^{eq}), as determined by charge neutrality at 973 K, is marked with a dotted vertical line.

Group-4 Doping: Ti, Zr, Hf

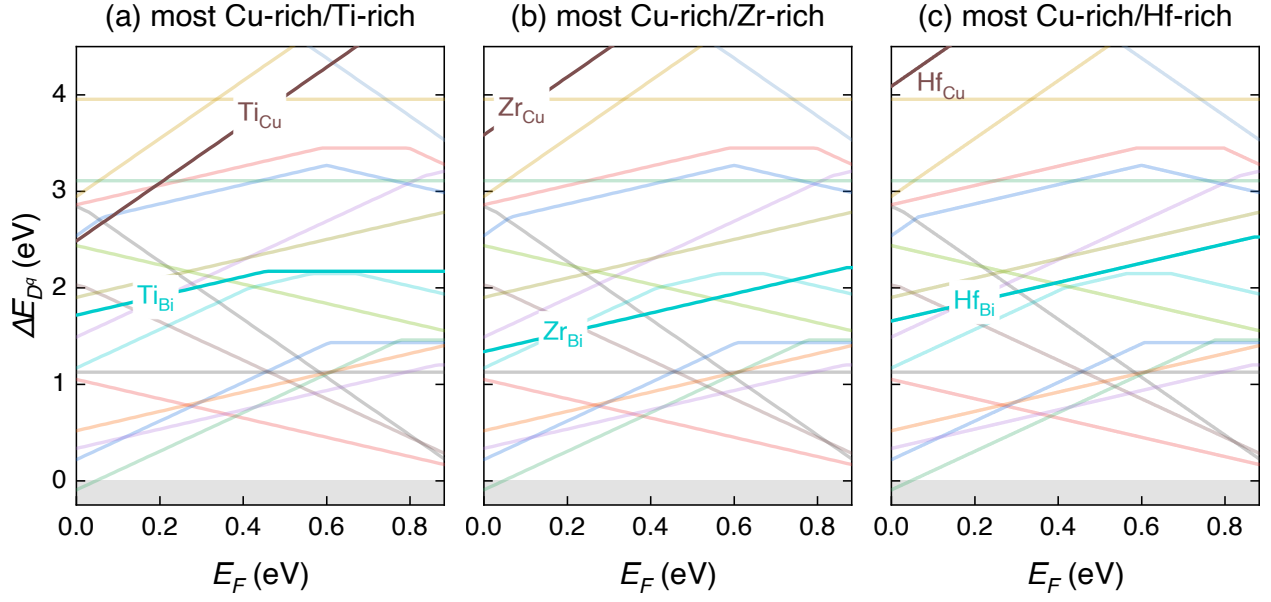


Figure S9: Formation energy of defects associated with (a) Ti, (b) Zr, and (c) Hf doping in BiCuSeO under Cu-rich conditions where BiCuSeO is in equilibrium with (a) Bi, Cu₂Se, Cu₂O, and Bi₂O₇Ti₂, (b) Bi, Cu₂Se, Cu₂O, and ZrO₂, and (c) Bi, Cu₂Se, Cu₂O, and HfO₂. Native defects of BiCuSeO (Figure 2 in main text) are shown in lighter colors. The equilibrium Fermi energy (E_F^{eq}), as determined by charge neutrality at 973 K, is marked with a dotted vertical line.

Group-13 Doping: Al, Ga, In, and Tl

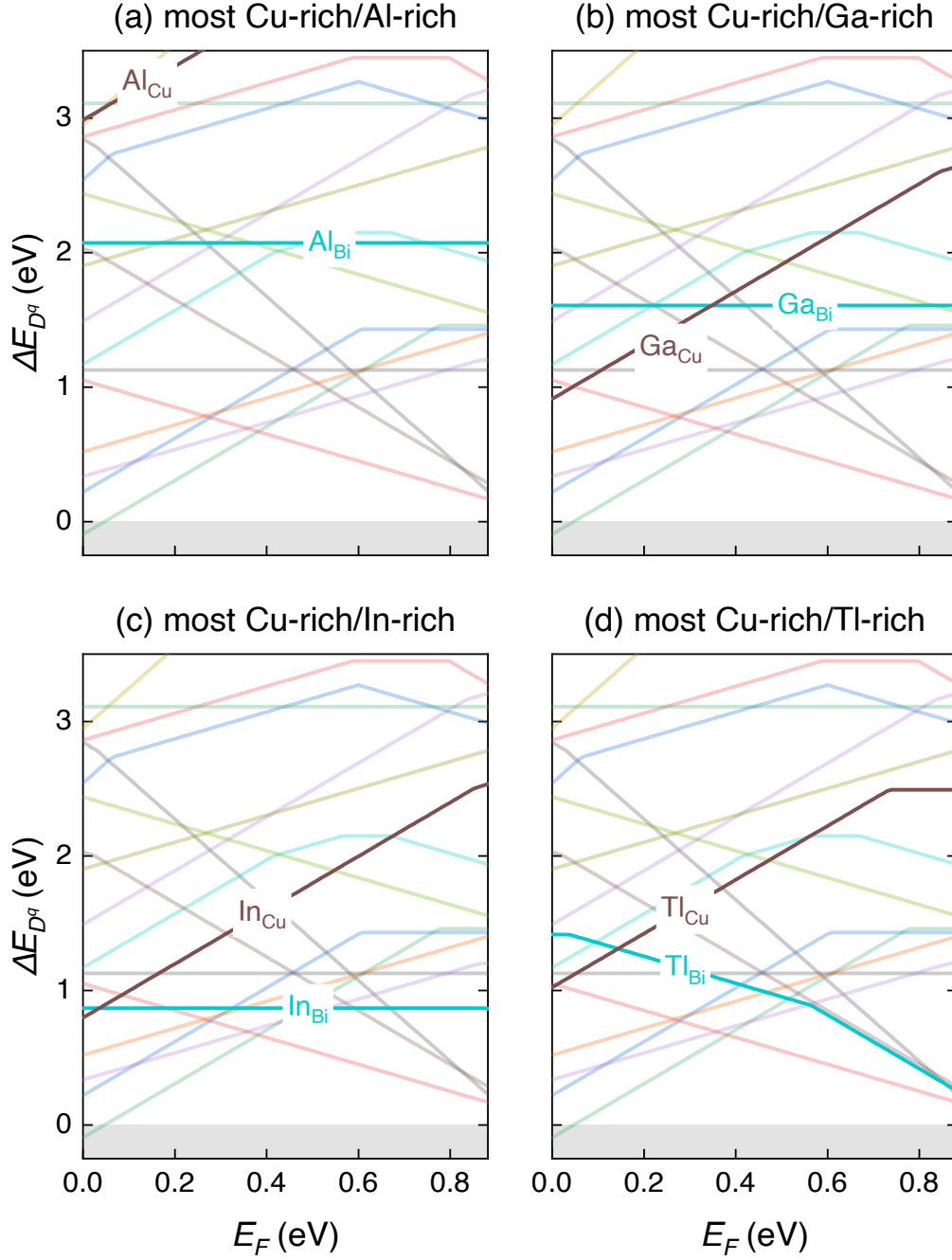


Figure S10: Formation energy of defects associated with (a) Al, (b) Ga, (c) In, and (d) Tl doping in BiCuSeO under Cu-rich conditions where BiCuSeO is in equilibrium with (a) Bi, Cu_2Se , Cu_2O , and AlCuO_2 , (b) Bi, Cu_2Se , Cu_2O , and CuGaO_2 , (c) Bi, Cu_2Se , Cu_2O , and CuInO_2 , and (d) Bi, Cu_2Se , Cu_2O , and $\text{Cu}_2\text{Se}_2\text{Tl}$. Native defects of BiCuSeO (Figure 2 in main text) are shown in lighter colors. The equilibrium Fermi energy (E_F^{eq}), as determined by charge neutrality at 973 K, is marked with a dotted vertical line.

Group-14 Doping: Si, Ge, Sn, Pb

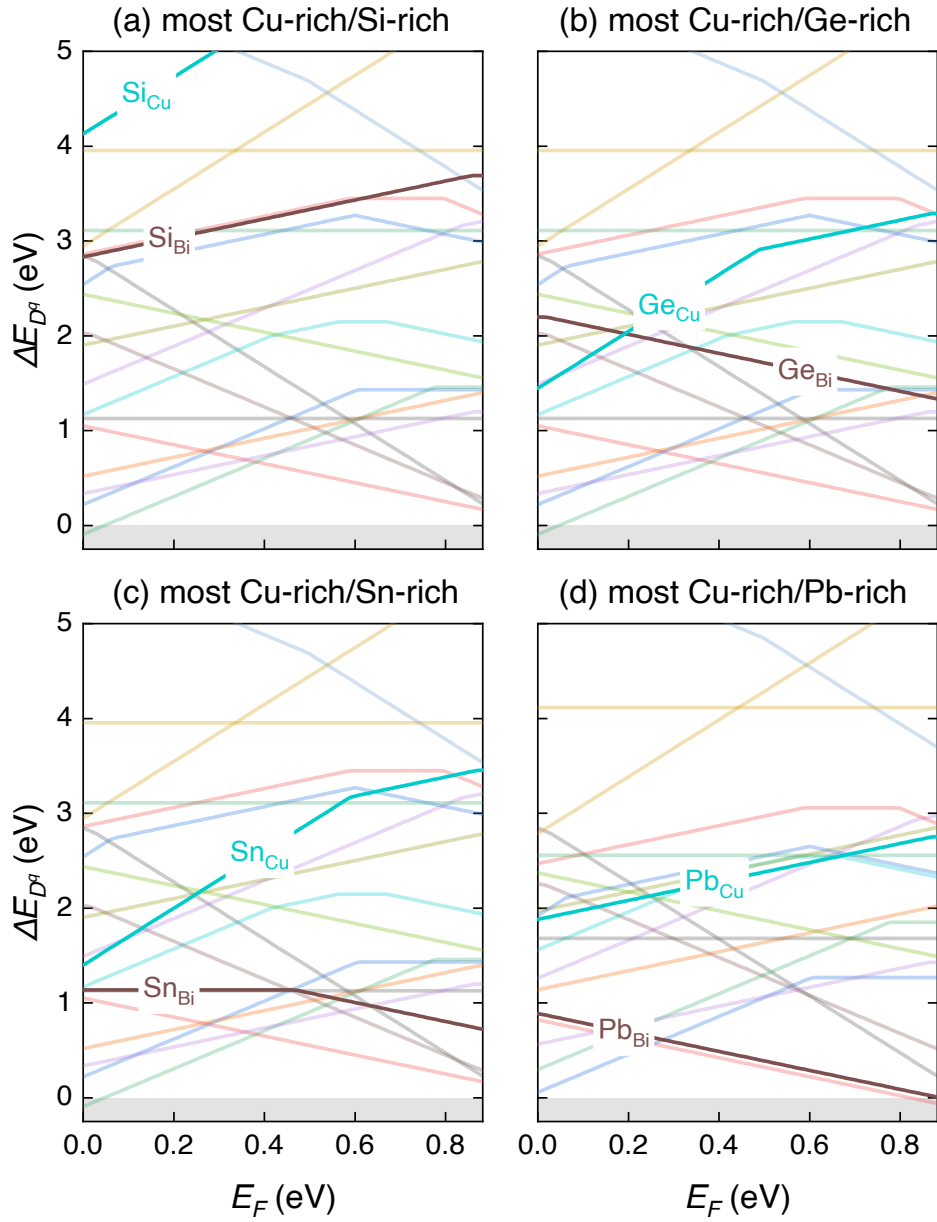


Figure S11: Formation energy of defects associated with (a) Si, (b) Ge, (c) Sn, and (d) Pb doping in BiCuSeO under Cu-rich conditions where BiCuSeO is in equilibrium with a) Bi, Cu₂Se, Cu₂O, and Bi₄O₁₂Si₃, (b) Bi, Cu₂Se, Cu₂O, and Bi₄Ge₃O₁₂, (c) Bi, Cu₂O, Bi₂O₇Sn₂, and Cu₂Se, and (d) Bi, PbSe, Cu₃Se₂, and Bi₂Se₃. Native defects of BiCuSeO (Figure 2 in main text) are shown in lighter colors. The equilibrium Fermi energy (E_F^{eq}), as determined by charge neutrality at 973 K, is marked with a dotted vertical line.

Phase Equilibria of Mg-Doped BiCuSeO

Equilibrium Phases	$\Delta\mu_{\text{Bi}}$	$\Delta\mu_{\text{Cu}}$	$\Delta\mu_{\text{Mg}}$	$\Delta\mu_{\text{O}}$	$\Delta\mu_{\text{Se}}$	$p - n \text{ (cm}^{-3}\text{)}$
Se, MgO, Cu ₃ Se ₂ , Bi ₂ Se ₃	-0.378	-0.62	-4.323	-1.923	0.0	7.39×10^{19}
Se, MgO, Bi ₂ O ₂ Se, Bi ₂ O ₃	-0.602	-0.708	-4.636	-1.61	0.0	1.26×10^{20}
Se, MgO, Bi ₂ O ₂ Se, Bi ₂ Se ₃	-0.378	-0.708	-4.411	-1.835	0.0	1.25×10^{20}
Se, MgO, Cu ₃ Se ₂ , Bi ₂ O ₃	-0.865	-0.62	-4.811	-1.435	0.0	7.53×10^{19}
Bi, MgO, Bi ₂ O ₂ Se, Bi ₂ Se ₃	0.0	-0.582	-4.159	-2.087	-0.252	5.39×10^{19}
Bi, Cu ₂ Se, MgO, Cu ₂ O	0.0	-0.223	-4.192	-2.054	-0.643	5.24×10^{18}
Bi, MgO, Cu ₂ O, Bi ₂ O ₃	0.0	-0.244	-4.234	-2.012	-0.664	5.67×10^{18}
Bi, MgO, Bi ₂ O ₂ Se, Bi ₂ O ₃	0.0	-0.507	-4.234	-2.012	-0.402	3.45×10^{19}
Bi, MgO, Cu ₃ Se ₂ , Bi ₂ Se ₃	0.0	-0.452	-4.03	-2.216	-0.252	2.36×10^{19}
Bi, Cu ₂ Se, MgO, Cu ₃ Se ₂	0.0	-0.318	-4.097	-2.149	-0.453	1.12×10^{19}
MgO, Cu ₃ Se ₂ , Cu ₂ O, Bi ₂ O ₃	-0.603	-0.445	-4.636	-1.61	-0.262	2.63×10^{19}
Cu ₂ Se, MgO, Cu ₃ Se ₂ , Cu ₂ O	-0.285	-0.318	-4.382	-1.864	-0.453	1.16×10^{19}

Table S4: Chemical potentials $\Delta\mu_i$ (in eV) in all phase regions of the quinary Bi-Cu-Se-O-Mg phase space that are in equilibrium with BiCuSeO. The corresponding charge carrier concentration in each phase region, as determined by charge neutrality at the typical synthesis temperature of 973 K, is listed.

Phase Equilibria of Ca-Doped BiCuSeO

Equilibrium Phases	$\Delta\mu_{\text{Bi}}$	$\Delta\mu_{\text{Ca}}$	$\Delta\mu_{\text{Cu}}$	$\Delta\mu_{\text{O}}$	$\Delta\mu_{\text{Se}}$	$p - n \text{ (cm}^{-3}\text{)}$
Se, CaO, Cu ₃ Se ₂ , Bi ₂ Se ₃	-0.378	-4.659	-0.62	-1.923	0.0	1.38×10^{21}
Se, CaO, CaO ₃ Se, Bi ₂ Se ₃	-0.378	-4.723	-0.684	-1.859	0.0	1.19×10^{21}
Se, Bi ₂ O ₂ Se, CaO ₃ Se, Bi ₂ Se ₃	-0.378	-4.795	-0.708	-1.835	0.0	8.89×10^{20}
Se, CaO, Cu ₃ Se ₂ , CaO ₃ Se	-0.441	-4.723	-0.62	-1.859	0.0	1.53×10^{21}
Se, Cu ₃ Se ₂ , Bi ₂ O ₃ , CaO ₃ Se	-0.865	-5.995	-0.62	-1.435	0.0	7.65×10^{19}
Se, Bi ₂ O ₂ Se, Bi ₂ O ₃ , CaO ₃ Se	-0.602	-5.47	-0.708	-1.61	0.0	1.45×10^{20}
Bi, CaO, Cu ₂ O, Bi ₂ O ₃	0.0	-4.57	-0.244	-2.012	-0.664	1.11×10^{20}
Bi, CaO, Cu ₂ Se, Cu ₂ O	0.0	-4.528	-0.223	-2.054	-0.643	1.41×10^{20}
Bi, CaO, Bi ₂ O ₂ Se, Bi ₂ Se ₃	0.0	-4.495	-0.582	-2.087	-0.252	3.88×10^{20}
Bi, CaO, Bi ₂ O ₂ Se, Bi ₂ O ₃	0.0	-4.57	-0.507	-2.012	-0.402	2.53×10^{20}
Bi, CaO, Cu ₃ Se ₂ , Bi ₂ Se ₃	0.0	-4.366	-0.452	-2.216	-0.252	4.48×10^{20}
Bi, CaO, Cu ₂ Se, Cu ₃ Se ₂	0.0	-4.433	-0.318	-2.149	-0.453	3.44×10^{20}
CaO, Bi ₂ O ₂ Se, CaO ₃ Se, Bi ₂ Se ₃	-0.354	-4.731	-0.7	-1.851	-0.016	1.05×10^{21}
CaO, Cu ₂ Se, Cu ₂ O, Cu ₃ Se ₂	-0.285	-4.718	-0.318	-1.864	-0.453	3.95×10^{20}
CaO, Bi ₂ O ₂ Se, Bi ₂ O ₃ , CaO ₃ Se	-0.353	-4.806	-0.625	-1.776	-0.166	7×10^{20}
CaO, Cu ₂ O, Bi ₂ O ₃ , CaO ₃ Se	-0.485	-4.894	-0.406	-1.688	-0.341	6.1×10^{20}
Cu ₂ O, Cu ₃ Se ₂ , Bi ₂ O ₃ , CaO ₃ Se	-0.603	-5.208	-0.445	-1.61	-0.262	2.97×10^{20}
CaO, Cu ₂ O, Cu ₃ Se ₂ , CaO ₃ Se	-0.496	-4.886	-0.402	-1.696	-0.327	6.81×10^{20}

Table S5: Chemical potentials $\Delta\mu_i$ (in eV) in all phase regions of the quinary Bi-Cu-Se-O-Ca phase space that are in equilibrium with BiCuSeO. The corresponding charge carrier concentration in each phase region, as determined by charge neutrality at the typical synthesis temperature of 973 K, is listed.

Phase Equilibria of Sr-Doped BiCuSeO

Equilibrium Phases	$\Delta\mu_{\text{Bi}}$	$\Delta\mu_{\text{Cu}}$	$\Delta\mu_{\text{O}}$	$\Delta\mu_{\text{Se}}$	$\Delta\mu_{\text{Sr}}$	$p - n \text{ (cm}^{-3}\text{)}$
Bi, SeSr, Cu ₃ Se ₂ , Bi ₂ Se ₃	0.0	-0.452	-2.216	-0.252	-4.274	5.95×10^{20}
Bi, Cu ₂ O, Bi ₂ O ₃ , Bi ₂ O ₄ Sr	0.0	-0.244	-2.012	-0.664	-4.72	5.66×10^{19}
Bi, Cu ₂ Se, Cu ₂ O, Bi ₂ O ₄ Sr	0.0	-0.223	-2.054	-0.643	-4.551	1.2×10^{20}
Bi, Cu ₂ Se, Bi ₂ O ₅ Sr ₂ , Bi ₂ O ₄ Sr	0.0	-0.258	-2.089	-0.573	-4.411	2.66×10^{20}
Bi, Cu ₂ Se, Bi ₂ O ₅ Sr ₂ , Cu ₃ Se ₂	0.0	-0.318	-2.149	-0.453	-4.261	6.19×10^{20}
Bi, SeSr, Bi ₂ O ₅ Sr ₂ , Cu ₃ Se ₂	0.0	-0.386	-2.183	-0.351	-4.175	8.91×10^{20}
O ₃ SeSr, SeSr, Cu ₃ Se ₂ , Bi ₂ Se ₃	-0.313	-0.591	-1.973	-0.043	-4.483	1.7×10^{21}
O ₃ SeSr, SeSr, Bi ₂ O ₅ Sr ₂ , Bi ₂ Se ₃	-0.256	-0.61	-1.973	-0.081	-4.445	1.59×10^{21}
O ₃ SeSr, Bi ₂ O ₅ Sr ₂ , Bi ₂ O ₄ Sr, Bi ₂ Se ₃	-0.242	-0.66	-1.927	-0.09	-4.573	1.05×10^{21}
O ₃ SeSr, Bi ₂ O ₂ Se, Bi ₂ O ₄ Sr, Bi ₂ Se ₃	-0.244	-0.663	-1.924	-0.089	-4.583	1.02×10^{21}
O ₃ SeSr, Cu ₂ O, Cu ₃ Se ₂ , Bi ₂ O ₄ Sr	-0.474	-0.394	-1.712	-0.339	-4.968	4.02×10^{20}
O ₃ SeSr, Bi ₂ O ₅ Sr ₂ , Cu ₃ Se ₂ , Bi ₂ O ₄ Sr	-0.371	-0.445	-1.842	-0.262	-4.658	1.09×10^{21}
O ₃ SeSr, Cu ₂ O, Cu ₃ Se ₂ , Bi ₂ O ₃	-0.603	-0.445	-1.61	-0.262	-5.353	1.29×10^{20}
O ₃ SeSr, SeSr, Bi ₂ O ₅ Sr ₂ , Cu ₃ Se ₂	-0.289	-0.544	-1.973	-0.114	-4.412	1.92×10^{21}
O ₃ SeSr, Bi ₂ O ₂ Se, Bi ₂ O ₃ , Bi ₂ O ₄ Sr	-0.356	-0.625	-1.774	-0.164	-4.958	3.1×10^{20}
O ₃ SeSr, Cu ₂ O, Bi ₂ O ₃ , Bi ₂ O ₄ Sr	-0.487	-0.407	-1.687	-0.339	-5.045	3.03×10^{20}
Cu ₂ Se, Bi ₂ O ₅ Sr ₂ , Cu ₃ Se ₂ , Bi ₂ O ₄ Sr	-0.18	-0.318	-1.969	-0.453	-4.531	5.04×10^{20}
Cu ₂ Se, Cu ₂ O, Cu ₃ Se ₂ , Bi ₂ O ₄ Sr	-0.285	-0.318	-1.864	-0.453	-4.741	3.4×10^{20}
Se, O ₃ SeSr, Bi ₂ O ₂ Se, Bi ₂ O ₃	-0.603	-0.708	-1.61	0.0	-5.615	1.29×10^{20}
Se, O ₃ SeSr, Cu ₃ Se ₂ , Bi ₂ O ₃	-0.865	-0.62	-1.435	0.0	-6.14	7.53×10^{19}
Se, O ₃ SeSr, Bi ₂ O ₂ Se, Bi ₂ Se ₃	-0.378	-0.708	-1.835	0.0	-4.94	4.03×10^{20}
Se, O ₃ SeSr, Cu ₃ Se ₂ , Bi ₂ Se ₃	-0.378	-0.62	-1.923	0.0	-4.677	1.22×10^{21}

Table S6: Chemical potentials $\Delta\mu_i$ (in eV) in all phase regions of the quinary Bi-Cu-Se-O-Sr phase space that are in equilibrium with BiCuSeO. The corresponding charge carrier concentration in each phase region, as determined by charge neutrality at the typical synthesis temperature of 973 K, is listed.

Phase Equilibria of Ba-Doped BiCuSeO

Equilibrium Phases	$\Delta\mu_{\text{Ba}}$	$\Delta\mu_{\text{Bi}}$	$\Delta\mu_{\text{Cu}}$	$\Delta\mu_{\text{O}}$	$\Delta\mu_{\text{Se}}$	$p - n \text{ (cm}^{-3}\text{)}$
Se, Bi ₂ Se ₃ , BaO ₃ Se, Cu ₃ Se ₂	-4.722	-0.378	-0.62	-1.923	0.0	8.82×10^{19}
Se, Bi ₂ Se ₃ , Bi ₂ O ₂ Se, BaO ₃ Se	-4.985	-0.378	-0.708	-1.835	0.0	1.25×10^{20}
Se, BaO ₃ Se, Cu ₃ Se ₂ , Bi ₂ O ₃	-6.185	-0.865	-0.62	-1.435	0.0	7.5×10^{19}
Se, Bi ₂ O ₂ Se, BaO ₃ Se, Bi ₂ O ₃	-5.66	-0.603	-0.708	-1.61	0.0	1.26×10^{20}
Bi ₂ Se ₃ , BaSe, BaBiSe ₃ , BaCu ₂ Se ₂	-4.399	-0.169	-0.609	-2.003	-0.139	1.12×10^{20}
Bi ₂ Se ₃ , BaCu ₂ Se ₂ , BaO ₃ Se, Cu ₃ Se ₂	-4.643	-0.351	-0.608	-1.943	-0.018	9.45×10^{19}
Bi ₂ Se ₃ , BaBiSe ₃ , BaCu ₂ Se ₂ , BaO ₃ Se	-4.448	-0.218	-0.617	-1.979	-0.106	1.16×10^{20}
Bi ₂ Se ₃ , BaSe, Bi ₂ O ₂ Se, BaO ₃ Se	-4.389	-0.154	-0.633	-1.984	-0.149	1.17×10^{20}
Bi ₂ Se ₃ , BaSe, BaBiSe ₃ , BaO ₃ Se	-4.399	-0.169	-0.628	-1.984	-0.139	1.18×10^{20}
Cu ₂ O, BaO ₃ Se, Cu ₃ Se ₂ , Ba ₂ Bi ₄ O ₈	-4.706	-0.372	-0.353	-1.795	-0.401	4.84×10^{19}
BaCu ₂ Se ₂ , BaO ₃ Se, Cu ₃ Se ₂ , Ba ₂ Bi ₄ O ₈	-4.433	-0.281	-0.398	-1.908	-0.333	1.33×10^{20}
Cu ₂ O, BaO ₃ Se, Cu ₃ Se ₂ , Bi ₂ O ₃	-5.398	-0.603	-0.445	-1.61	-0.262	2.62×10^{19}
Cu ₂ O, BaO ₃ Se, Bi ₂ O ₃ , Ba ₂ Bi ₄ O ₈	-4.844	-0.395	-0.376	-1.748	-0.401	2.94×10^{19}
Bi ₂ O ₂ Se, BaO ₃ Se, Bi ₂ O ₃ , Ba ₂ Bi ₄ O ₈	-4.757	-0.264	-0.595	-1.836	-0.226	6.61×10^{19}
BaSe, Bi ₂ O ₂ Se, BaO ₃ Se, Ba ₂ Bi ₄ O ₈	-4.386	-0.153	-0.632	-1.984	-0.152	1.17×10^{20}
BaSe, BaCu ₂ Se ₂ , BaO ₃ Se, Ba ₂ Bi ₄ O ₈	-4.357	-0.167	-0.588	-1.984	-0.181	1.28×10^{20}
BaSe, BaBiSe ₃ , BaCu ₂ Se ₂ , BaO ₃ Se	-4.412	-0.194	-0.615	-1.984	-0.126	1.2×10^{20}
BaCu ₂ Se ₂ , Cu ₃ Se ₂ , Cu ₂ Se, Ba ₂ Bi ₄ O ₈	-4.353	-0.161	-0.318	-1.988	-0.453	8.68×10^{19}
Cu ₂ O, Cu ₃ Se ₂ , Cu ₂ Se, Ba ₂ Bi ₄ O ₈	-4.601	-0.285	-0.318	-1.864	-0.453	4.84×10^{19}
Bi, Cu ₂ O, Cu ₂ Se, Ba ₂ Bi ₄ O ₈	-4.411	0.0	-0.223	-2.054	-0.643	1.93×10^{19}
Bi, BaCu ₂ Se ₂ , Cu ₂ Se, Ba ₂ Bi ₄ O ₈	-4.246	0.0	-0.264	-2.095	-0.56	5.07×10^{19}
Bi, Cu ₂ O, Bi ₂ O ₃ , Ba ₂ Bi ₄ O ₈	-4.581	0.0	-0.244	-2.012	-0.664	9.38×10^{18}
Bi, BaCu ₂ Se ₂ , Cu ₃ Se ₂ , Cu ₂ Se	-4.353	0.0	-0.318	-2.149	-0.453	3.76×10^{19}
Bi, Bi ₂ Se ₃ , BaCu ₂ Se ₂ , Cu ₃ Se ₂	-4.487	0.0	-0.452	-2.216	-0.252	2.87×10^{19}
Bi, BaSe, BaCu ₂ Se ₂ , Ba ₂ Bi ₄ O ₈	-4.246	0.0	-0.532	-2.095	-0.292	8.36×10^{19}
Bi, Bi ₂ O ₂ Se, Bi ₂ O ₃ , Ba ₂ Bi ₄ O ₈	-4.581	0.0	-0.507	-2.012	-0.402	3.6×10^{19}
Bi, BaSe, Bi ₂ O ₂ Se, Ba ₂ Bi ₄ O ₈	-4.284	0.0	-0.581	-2.086	-0.254	8.02×10^{19}
Bi, Bi ₂ Se ₃ , BaSe, Bi ₂ O ₂ Se	-4.286	0.0	-0.582	-2.087	-0.252	8×10^{19}
Bi, Bi ₂ Se ₃ , BaSe, BaCu ₂ Se ₂	-4.286	0.0	-0.553	-2.116	-0.252	7.29×10^{19}

Table S7: Chemical potentials $\Delta\mu_i$ (in eV) in all phase regions of the quinary Bi-Cu-Se-O-Ba phase space that are in equilibrium with BiCuSeO. The corresponding charge carrier concentration in each phase region, as determined by charge neutrality at the typical synthesis temperature of 973 K, is listed.

Phase Equilibria of Li-Doped BiCuSeO

Equilibrium Phases	$\Delta\mu_{\text{Bi}}$	$\Delta\mu_{\text{Cu}}$	$\Delta\mu_{\text{Li}}$	$\Delta\mu_{\text{O}}$	$\Delta\mu_{\text{Se}}$	$p - n \text{ (cm}^{-3}\text{)}$
Se, Cu ₃ Se ₂ , Bi ₂ Se ₃ , Bi ₈ Li ₂₄ O ₂₄	-0.378	-0.62	-2.217	-1.923	0.0	1.12×10^{20}
Se, Bi ₂ O ₂ Se, Bi ₂ O ₃ , BiLiO ₂	-0.603	-0.708	-2.509	-1.61	0.0	1.44×10^{20}
Se, Bi ₂ O ₂ Se, BiLiO ₂ , Bi ₈ Li ₂₄ O ₂₄	-0.438	-0.708	-2.345	-1.775	0.0	1.22×10^{20}
Se, Bi ₂ O ₂ Se, Bi ₂ Se ₃ , Bi ₈ Li ₂₄ O ₂₄	-0.378	-0.708	-2.305	-1.835	0.0	1.09×10^{20}
Se, Li ₄ O ₅ Se, Cu ₃ Se ₂ , Bi ₈ Li ₂₄ O ₂₄	-0.609	-0.62	-2.372	-1.691	0.0	1.75×10^{20}
Se, Li ₄ O ₅ Se, Cu ₃ Se ₂ , Bi ₂ O ₃	-0.865	-0.62	-2.691	-1.435	0.0	1.48×10^{20}
Se, Li ₄ O ₅ Se, BiLiO ₂ , Bi ₈ Li ₂₄ O ₂₄	-0.594	-0.655	-2.397	-1.671	0.0	1.57×10^{20}
Se, Li ₄ O ₅ Se, Bi ₂ O ₃ , BiLiO ₂	-0.676	-0.683	-2.534	-1.561	0.0	1.48×10^{20}
Bi, Bi ₂ O ₂ Se, Bi ₂ Se ₃ , Bi ₈ Li ₂₄ O ₂₄	0.0	-0.582	-2.179	-2.087	-0.252	4.61×10^{19}
Bi, BiLiO ₂ , Cu ₈ Li ₈ O ₈ , Bi ₈ Li ₂₄ O ₂₄	0.0	-0.329	-2.199	-2.067	-0.525	2.62×10^{19}
Bi, Bi ₂ O ₂ Se, BiLiO ₂ , Bi ₈ Li ₂₄ O ₂₄	0.0	-0.562	-2.199	-2.067	-0.292	4.48×10^{19}
Bi, Bi ₂ O ₂ Se, Bi ₂ O ₃ , BiLiO ₂	0.0	-0.507	-2.309	-2.012	-0.402	3.57×10^{19}
Bi, Bi ₂ O ₃ , BiLiO ₂ , Cu ₈ Li ₈ O ₈	0.0	-0.274	-2.309	-2.012	-0.634	1.53×10^{19}
Bi, Cu ₂ O, Bi ₂ O ₃ , Cu ₈ Li ₈ O ₈	0.0	-0.244	-2.338	-2.012	-0.664	1.28×10^{19}
Bi, Cu ₂ Se, Cu ₂ O, Cu ₈ Li ₈ O ₈	0.0	-0.223	-2.317	-2.054	-0.643	1.41×10^{19}
Bi, Cu ₃ Se ₂ , Bi ₂ Se ₃ , Bi ₈ Li ₂₄ O ₂₄	0.0	-0.452	-2.049	-2.216	-0.252	4.26×10^{19}
Bi, Cu ₂ Se, Cu ₃ Se ₂ , Cu ₈ Li ₈ O ₈	0.0	-0.318	-2.127	-2.149	-0.453	3.45×10^{19}
Bi, Cu ₃ Se ₂ , Cu ₈ Li ₈ O ₈ , Bi ₈ Li ₂₄ O ₂₄	0.0	-0.329	-2.111	-2.155	-0.437	3.66×10^{19}
Cu ₃ Se ₂ , BiLiO ₂ , Cu ₈ Li ₈ O ₈ , Bi ₈ Li ₂₄ O ₂₄	-0.527	-0.505	-2.375	-1.715	-0.173	1.23×10^{20}
Cu ₃ Se ₂ , Bi ₂ O ₃ , BiLiO ₂ , Cu ₈ Li ₈ O ₈	-0.692	-0.505	-2.539	-1.55	-0.173	1.25×10^{20}
Cu ₂ O, Cu ₃ Se ₂ , Bi ₂ O ₃ , Cu ₈ Li ₈ O ₈	-0.603	-0.445	-2.539	-1.61	-0.262	8.63×10^{19}
Li ₄ O ₅ Se, Cu ₃ Se ₂ , Bi ₂ O ₃ , BiLiO ₂	-0.739	-0.536	-2.555	-1.519	-0.126	1.43×10^{20}
Li ₄ O ₅ Se, Cu ₃ Se ₂ , BiLiO ₂ , Bi ₈ Li ₂₄ O ₂₄	-0.63	-0.573	-2.409	-1.647	-0.071	1.65×10^{20}
Cu ₂ Se, Cu ₂ O, Cu ₃ Se ₂ , Cu ₈ Li ₈ O ₈	-0.285	-0.318	-2.412	-1.864	-0.453	3.66×10^{19}

Table S8: Chemical potentials $\Delta\mu_i$ (in eV) in all phase regions of the quinary Bi-Cu-Se-O-Li phase space that are in equilibrium with BiCuSeO. The corresponding charge carrier concentration in each phase region, as determined by charge neutrality at the typical synthesis temperature of 973 K, is listed.

Phase Equilibria of Zn-Doped BiCuSeO

Equilibrium Phases	$\Delta\mu_{\text{Bi}}$	$\Delta\mu_{\text{Cu}}$	$\Delta\mu_{\text{O}}$	$\Delta\mu_{\text{Se}}$	$\Delta\mu_{\text{Zn}}$	$p - n \text{ (cm}^{-3}\text{)}$
Bi, Bi ₂ O ₂ Se, Bi ₂ Se ₃ , SeZn	0.0	-0.582	-2.087	-0.252	-1.496	6.54×10^{18}
Bi, Bi ₂ O ₂ Se, SeZn, OZn	0.0	-0.579	-2.084	-0.256	-1.492	6.37×10^{18}
Bi, Cu ₂ Se, Cu ₂ O, OZn	0.0	-0.223	-2.054	-0.643	-1.522	4.3×10^{18}
Bi, Cu ₂ O, Bi ₂ O ₃ , OZn	0.0	-0.244	-2.012	-0.664	-1.564	4.94×10^{18}
Bi, Bi ₂ O ₂ Se, Bi ₂ O ₃ , OZn	0.0	-0.507	-2.012	-0.402	-1.564	9.63×10^{18}
Bi, Bi ₂ Se ₃ , Cu ₃ Se ₂ , SeZn	0.0	-0.452	-2.216	-0.252	-1.496	6.37×10^{18}
Bi, Cu ₃ Se ₂ , SeZn, OZn	0.0	-0.384	-2.182	-0.354	-1.394	3.33×10^{18}
Bi, Cu ₂ Se, Cu ₃ Se ₂ , OZn	0.0	-0.318	-2.149	-0.453	-1.427	3.99×10^{18}
Cu ₂ Se, Cu ₂ O, Cu ₃ Se ₂ , OZn	-0.285	-0.318	-1.864	-0.453	-1.712	1.04×10^{19}
Cu ₂ O, Cu ₃ Se ₂ , Bi ₂ O ₃ , OZn	-0.603	-0.445	-1.61	-0.262	-1.966	2.55×10^{19}
Se, Cu ₃ Se ₂ , Bi ₂ O ₃ , OZn	-0.865	-0.62	-1.435	0.0	-2.141	7.29×10^{19}
Se, Bi ₂ O ₂ Se, Bi ₂ Se ₃ , SeZn	-0.378	-0.708	-1.835	0.0	-1.748	2.89×10^{19}
Se, Bi ₂ O ₂ Se, SeZn, OZn	-0.385	-0.708	-1.828	0.0	-1.748	2.89×10^{19}
Se, Bi ₂ O ₂ Se, Bi ₂ O ₃ , OZn	-0.603	-0.708	-1.61	0.0	-1.966	8.07×10^{19}
Se, Bi ₂ Se ₃ , Cu ₃ Se ₂ , SeZn	-0.378	-0.62	-1.923	0.0	-1.748	2.76×10^{19}
Se, Cu ₃ Se ₂ , SeZn, OZn	-0.472	-0.62	-1.828	0.0	-1.748	2.77×10^{19}

Table S9: Chemical potentials $\Delta\mu_i$ (in eV) in all phase regions of the quinary Bi-Cu-Se-O-Zn phase space that are in equilibrium with BiCuSeO. The corresponding charge carrier concentration in each phase region, as determined by charge neutrality at the typical synthesis temperature of 973 K, is listed.

Phase Equilibria of Al-Doped BiCuSeO

Equilibrium Phases	$\Delta\mu_{\text{Al}}$	$\Delta\mu_{\text{Bi}}$	$\Delta\mu_{\text{Cu}}$	$\Delta\mu_{\text{O}}$	$\Delta\mu_{\text{Se}}$	$p - n \text{ (cm}^{-3}\text{)}$
Se, Al ₂ O ₃ , Bi ₂ Se ₃ , Cu ₃ Se ₂	-5.916	-0.378	-0.62	-1.923	0.0	7.36×10^{19}
Se, Bi ₂ O ₂ Se, Bi ₂ O ₃ , Al ₄ Bi ₂ O ₉	-6.484	-0.602	-0.708	-1.61	0.0	1.26×10^{20}
Se, Bi ₂ O ₂ Se, Bi ₂ Se ₃ , Al ₄ Bi ₂ O ₉	-6.09	-0.378	-0.708	-1.835	0.0	1.25×10^{20}
Se, Al ₂ O ₃ , Bi ₂ Se ₃ , Al ₄ Bi ₂ O ₉	-5.962	-0.378	-0.651	-1.892	0.0	8.88×10^{19}
Se, Al ₂ O ₃ , Cu ₃ Se ₂ , Al ₄ Bi ₂ O ₉	-6.055	-0.47	-0.62	-1.83	0.0	7.46×10^{19}
Se, Cu ₃ Se ₂ , Bi ₂ O ₃ , Al ₄ Bi ₂ O ₉	-6.746	-0.865	-0.62	-1.435	0.0	7.5×10^{19}
Cu ₂ O, Cu ₃ Se ₂ , AlCuO ₂ , Bi ₂ O ₃	-6.523	-0.603	-0.445	-1.61	-0.262	2.61×10^{19}
Cu ₃ Se ₂ , AlCuO ₂ , Bi ₂ O ₃ , Al ₄ Bi ₂ O ₉	-6.602	-0.721	-0.524	-1.531	-0.145	4.22×10^{19}
Al ₂ O ₃ , Cu ₃ Se ₂ , AlCuO ₂ , Al ₄ Bi ₂ O ₉	-5.614	-0.029	-0.326	-2.124	-0.441	1.17×10^{19}
Cu ₂ Se, Cu ₂ O, Cu ₃ Se ₂ , AlCuO ₂	-6.142	-0.285	-0.318	-1.864	-0.453	1.13×10^{19}
Cu ₂ Se, Al ₂ O ₃ , Cu ₃ Se ₂ , AlCuO ₂	-5.59	-0.009	-0.318	-2.14	-0.453	1.1×10^{19}
Bi, Cu ₂ Se, Al ₂ O ₃ , Cu ₃ Se ₂	-5.576	0.0	-0.318	-2.149	-0.453	1.1×10^{19}
Bi, Al ₂ O ₃ , Bi ₂ Se ₃ , Cu ₃ Se ₂	-5.476	0.0	-0.452	-2.216	-0.252	2.34×10^{19}
Bi, Cu ₂ Se, Cu ₂ O, AlCuO ₂	-5.857	0.0	-0.223	-2.054	-0.643	5.11×10^{18}
Bi, Cu ₂ Se, Al ₂ O ₃ , AlCuO ₂	-5.581	0.0	-0.315	-2.146	-0.459	1.08×10^{19}
Bi, Al ₂ O ₃ , AlCuO ₂ , Al ₄ Bi ₂ O ₉	-5.585	0.0	-0.316	-2.143	-0.46	1.08×10^{19}
Bi, AlCuO ₂ , Bi ₂ O ₃ , Al ₄ Bi ₂ O ₉	-5.881	0.0	-0.283	-2.012	-0.625	7.59×10^{18}
Bi, Cu ₂ O, AlCuO ₂ , Bi ₂ O ₃	-5.92	0.0	-0.244	-2.012	-0.664	5.61×10^{18}
Bi, Bi ₂ O ₂ Se, Bi ₂ O ₃ , Al ₄ Bi ₂ O ₉	-5.881	0.0	-0.507	-2.012	-0.402	3.45×10^{19}
Bi, Bi ₂ O ₂ Se, Bi ₂ Se ₃ , Al ₄ Bi ₂ O ₉	-5.712	0.0	-0.582	-2.087	-0.252	5.39×10^{19}
Bi, Al ₂ O ₃ , Bi ₂ Se ₃ , Al ₄ Bi ₂ O ₉	-5.585	0.0	-0.525	-2.143	-0.252	3.77×10^{19}

Table S10: Chemical potentials $\Delta\mu_i$ (in eV) in all phase regions of the quinary Bi-Cu-Se-O-Al phase space that are in equilibrium with BiCuSeO. The corresponding charge carrier concentration in each phase region, as determined by charge neutrality at the typical synthesis temperature of 973 K, is listed.

Phase Equilibria of Ga-Doped BiCuSeO

Equilibrium Phases	$\Delta\mu_{\text{Bi}}$	$\Delta\mu_{\text{Cu}}$	$\Delta\mu_{\text{Ga}}$	$\Delta\mu_{\text{O}}$	$\Delta\mu_{\text{Se}}$	$p - n \text{ (cm}^{-3}\text{)}$
Se, Cu ₃ Se ₂ , Ga ₂ O ₃ , Bi ₂ Se ₃	-0.378	-0.62	-2.811	-1.923	0.0	7.36×10^{19}
Se, Bi ₂ O ₂ Se, Bi ₂ Ga ₄ O ₉ , Bi ₂ O ₃	-0.602	-0.708	-3.341	-1.61	0.0	1.26×10^{20}
Se, Bi ₂ Ga ₄ O ₉ , Ga ₂ O ₃ , Bi ₂ Se ₃	-0.378	-0.701	-2.933	-1.842	0.0	1.19×10^{20}
Se, Bi ₂ O ₂ Se, Bi ₂ Ga ₄ O ₉ , Bi ₂ Se ₃	-0.378	-0.708	-2.948	-1.835	0.0	1.24×10^{20}
Se, Bi ₂ Ga ₄ O ₉ , Cu ₃ Se ₂ , Ga ₂ O ₃	-0.62	-0.62	-3.175	-1.68	0.0	7.48×10^{19}
Se, Bi ₂ Ga ₄ O ₉ , Cu ₃ Se ₂ , Bi ₂ O ₃	-0.865	-0.62	-3.604	-1.435	0.0	7.5×10^{19}
Bi, Cu ₂ O, CuGaO ₂ , Bi ₂ O ₃	0.0	-0.244	-2.754	-2.012	-0.664	5.61×10^{18}
Bi, Bi ₂ O ₂ Se, Bi ₂ Ga ₄ O ₉ , Bi ₂ Se ₃	0.0	-0.582	-2.57	-2.087	-0.252	5.37×10^{19}
Bi, Bi ₂ Ga ₄ O ₉ , Ga ₂ O ₃ , Bi ₂ Se ₃	0.0	-0.575	-2.555	-2.093	-0.252	5.14×10^{19}
Bi, Bi ₂ O ₂ Se, Bi ₂ Ga ₄ O ₉ , Bi ₂ O ₃	0.0	-0.507	-2.739	-2.012	-0.402	3.45×10^{19}
Bi, CuGaO ₂ , Bi ₂ Ga ₄ O ₉ , Ga ₂ O ₃	0.0	-0.28	-2.555	-2.093	-0.546	8.27×10^{18}
Bi, CuGaO ₂ , Bi ₂ Ga ₄ O ₉ , Bi ₂ O ₃	0.0	-0.26	-2.739	-2.012	-0.648	6.37×10^{18}
Bi, Cu ₂ Se, CuGaO ₂ , Ga ₂ O ₃	0.0	-0.274	-2.537	-2.105	-0.54	8×10^{18}
Bi, Cu ₂ Se, Cu ₂ O, CuGaO ₂	0.0	-0.223	-2.691	-2.054	-0.643	5.11×10^{18}
Bi, Cu ₃ Se ₂ , Ga ₂ O ₃ , Bi ₂ Se ₃	0.0	-0.452	-2.371	-2.216	-0.252	2.33×10^{19}
Bi, Cu ₂ Se, Cu ₃ Se ₂ , Ga ₂ O ₃	0.0	-0.318	-2.471	-2.149	-0.453	1.1×10^{19}
CuGaO ₂ , Bi ₂ Ga ₄ O ₉ , Cu ₃ Se ₂ , Ga ₂ O ₃	-0.221	-0.354	-2.776	-1.946	-0.399	1.44×10^{19}
CuGaO ₂ , Bi ₂ Ga ₄ O ₉ , Cu ₃ Se ₂ , Bi ₂ O ₃	-0.65	-0.477	-3.389	-1.578	-0.215	3.17×10^{19}
Cu ₂ O, CuGaO ₂ , Cu ₃ Se ₂ , Bi ₂ O ₃	-0.603	-0.445	-3.357	-1.61	-0.262	2.61×10^{19}
Cu ₂ Se, Cu ₂ O, CuGaO ₂ , Cu ₃ Se ₂	-0.285	-0.318	-2.976	-1.864	-0.453	1.13×10^{19}
Cu ₂ Se, CuGaO ₂ , Cu ₃ Se ₂ , Ga ₂ O ₃	-0.131	-0.318	-2.668	-2.018	-0.453	1.13×10^{19}

Table S11: Chemical potentials $\Delta\mu_i$ (in eV) in all phase regions of the quinary Bi-Cu-Se-O-Ga phase space that are in equilibrium with BiCuSeO. The corresponding charge carrier concentration in each phase region, as determined by charge neutrality at the typical synthesis temperature of 973 K, is listed.

Phase Equilibria of In-Doped BiCuSeO

Equilibrium Phases	$\Delta\mu_{\text{Bi}}$	$\Delta\mu_{\text{Cu}}$	$\Delta\mu_{\text{In}}$	$\Delta\mu_{\text{O}}$	$\Delta\mu_{\text{Se}}$	$p - n \text{ (cm}^{-3}\text{)}$
Se, In_2O_3 , Cu_3Se_2 , CuInSe_2	-0.379	-0.62	-1.896	-1.921	0.0	7.34×10^{19}
Se, Cu_3Se_2 , CuInSe_2 , Bi_2Se_3	-0.378	-0.62	-1.896	-1.923	0.0	7.34×10^{19}
Se, In_2O_3 , $\text{Bi}_2\text{O}_2\text{Se}$, Bi_2O_3	-0.602	-0.708	-2.362	-1.61	0.0	1.26×10^{20}
Se, In_2O_3 , CuInSe_2 , Bi_2Se_3	-0.378	-0.621	-1.895	-1.922	0.0	7.39×10^{19}
Se, In_2O_3 , $\text{Bi}_2\text{O}_2\text{Se}$, Bi_2Se_3	-0.378	-0.708	-2.025	-1.835	0.0	1.24×10^{20}
Se, In_2O_3 , Cu_3Se_2 , Bi_2O_3	-0.865	-0.62	-2.625	-1.435	0.0	7.48×10^{19}
Bi, In_2O_3 , $\text{Bi}_2\text{O}_2\text{Se}$, Bi_2Se_3	0.0	-0.582	-1.648	-2.087	-0.252	5.36×10^{19}
Bi, In_2O_3 , CuInSe_2 , Bi_2Se_3	0.0	-0.495	-1.518	-2.173	-0.252	3.08×10^{19}
Bi, In_2O_3 , $\text{Bi}_2\text{O}_2\text{Se}$, Bi_2O_3	0.0	-0.507	-1.76	-2.012	-0.402	3.45×10^{19}
Bi, Cu_2Se , In_2O_3 , CuInO_2	0.0	-0.223	-1.696	-2.054	-0.642	5.13×10^{18}
Bi, Cu_2Se , Cu_2O , CuInO_2	0.0	-0.223	-1.697	-2.054	-0.643	5.11×10^{18}
Bi, Cu_2O , CuInO_2 , Bi_2O_3	0.0	-0.244	-1.76	-2.012	-0.664	5.61×10^{18}
Bi, In_2O_3 , CuInO_2 , Bi_2O_3	0.0	-0.245	-1.76	-2.012	-0.664	5.65×10^{18}
Bi, Cu_3Se_2 , CuInSe_2 , Bi_2Se_3	0.0	-0.452	-1.56	-2.216	-0.252	2.33×10^{19}
Bi, In_2O_3 , Cu_3Se_2 , CuInSe_2	0.0	-0.413	-1.482	-2.197	-0.31	1.91×10^{19}
Bi, Cu_2Se , In_2O_3 , Cu_3Se_2	0.0	-0.318	-1.554	-2.149	-0.453	1.1×10^{19}
In_2O_3 , CuInO_2 , Cu_3Se_2 , Bi_2O_3	-0.604	-0.446	-2.364	-1.609	-0.261	2.62×10^{19}
Cu_2O , CuInO_2 , Cu_3Se_2 , Bi_2O_3	-0.603	-0.445	-2.363	-1.61	-0.262	2.6×10^{19}
Cu_2Se , In_2O_3 , CuInO_2 , Cu_3Se_2	-0.284	-0.318	-1.98	-1.865	-0.453	1.13×10^{19}
Cu_2Se , Cu_2O , CuInO_2 , Cu_3Se_2	-0.285	-0.318	-1.982	-1.864	-0.453	1.13×10^{19}

Table S12: Chemical potentials $\Delta\mu_i$ (in eV) in all phase regions of the quinary Bi-Cu-Se-O-In phase space that are in equilibrium with BiCuSeO. The corresponding charge carrier concentration in each phase region, as determined by charge neutrality at the typical synthesis temperature of 973 K, is listed.

Phase Equilibria of Tl-Doped BiCuSeO

Equilibrium Phases	$\Delta\mu_{\text{Bi}}$	$\Delta\mu_{\text{Cu}}$	$\Delta\mu_{\text{O}}$	$\Delta\mu_{\text{Se}}$	$\Delta\mu_{\text{Tl}}$	$p - n \text{ (cm}^{-3}\text{)}$
Bi, Bi ₂ O ₂ Se, BiSe ₂ Tl, Bi ₂ Se ₃	0.0	-0.582	-2.087	-0.252	-0.659	5.39×10^{19}
Bi, BiSe ₂ Tl, Bi ₂ O ₃ , Se ₁₂ Tl ₂₀	0.0	-0.41	-2.012	-0.498	-0.166	1.85×10^{19}
Bi, Bi ₂ O ₂ Se, BiSe ₂ Tl, Bi ₂ O ₃	0.0	-0.507	-2.012	-0.402	-0.359	3.45×10^{19}
Bi, BiSe ₂ Tl, Cu ₃ Se ₂ , Bi ₂ Se ₃	0.0	-0.452	-2.216	-0.252	-0.659	2.34×10^{19}
Bi, BiSe ₂ Tl, Se ₁₂ Tl ₂₀ , Cu ₂ Se ₂ Tl	0.0	-0.399	-2.023	-0.498	-0.166	1.74×10^{19}
Bi, Bi ₂ O ₃ , Se ₁₂ Tl ₂₀ , Cu ₂ Se ₂ Tl	0.0	-0.372	-2.012	-0.537	-0.142	1.43×10^{19}
Bi, Cu ₂ O, Bi ₂ O ₃ , Cu ₂ Se ₂ Tl	0.0	-0.244	-2.012	-0.664	-0.142	5.67×10^{18}
Bi, Cu ₂ Se, Cu ₂ O, Cu ₂ Se ₂ Tl	0.0	-0.223	-2.054	-0.643	-0.227	5.15×10^{18}
Bi, BiSe ₂ Tl, Cu ₃ Se ₂ , Cu ₂ Se ₂ Tl	0.0	-0.399	-2.189	-0.332	-0.498	1.78×10^{19}
Bi, Cu ₂ Se, Cu ₃ Se ₂ , Cu ₂ Se ₂ Tl	0.0	-0.318	-2.149	-0.453	-0.417	1.1×10^{19}
BiSe ₂ Tl, Bi ₂ O ₃ , Se ₁₂ Tl ₂₀ , Cu ₂ Se ₂ Tl	-0.097	-0.447	-1.947	-0.429	-0.207	2.44×10^{19}
Cu ₂ Se, Cu ₂ O, Cu ₃ Se ₂ , Cu ₂ Se ₂ Tl	-0.285	-0.318	-1.864	-0.453	-0.417	1.14×10^{19}
Cu ₂ O, Cu ₃ Se ₂ , Bi ₂ O ₃ , Cu ₂ Se ₂ Tl	-0.603	-0.445	-1.61	-0.262	-0.544	2.62×10^{19}
Se, Cu ₃ Se ₂ , Bi ₂ O ₃ , Cu ₂ Se ₂ Tl	-0.865	-0.62	-1.435	0.0	-0.719	7.53×10^{19}
Se, BiSe ₂ Tl, Bi ₂ O ₃ , Cu ₂ Se ₂ Tl	-0.612	-0.704	-1.604	0.0	-0.55	1.23×10^{20}
Se, Bi ₂ O ₂ Se, BiSe ₂ Tl, Bi ₂ Se ₃	-0.378	-0.708	-1.835	0.0	-0.784	1.25×10^{20}
Se, Bi ₂ O ₂ Se, BiSe ₂ Tl, Bi ₂ O ₃	-0.602	-0.708	-1.61	0.0	-0.56	1.26×10^{20}
Se, BiSe ₂ Tl, Cu ₃ Se ₂ , Bi ₂ Se ₃	-0.378	-0.62	-1.923	0.0	-0.784	7.36×10^{19}
Se, BiSe ₂ Tl, Cu ₃ Se ₂ , Cu ₂ Se ₂ Tl	-0.443	-0.62	-1.857	0.0	-0.719	7.43×10^{19}

Table S13: Chemical potentials $\Delta\mu_i$ (in eV) in all phase regions of the quinary Bi-Cu-Se-O-Tl phase space that are in equilibrium with BiCuSeO. The corresponding charge carrier concentration in each phase region, as determined by charge neutrality at the typical synthesis temperature of 973 K, is listed.

Phase Equilibria of Si-Doped BiCuSeO

Equilibrium Phases	$\Delta\mu_{\text{Bi}}$	$\Delta\mu_{\text{Cu}}$	$\Delta\mu_{\text{O}}$	$\Delta\mu_{\text{Se}}$	$\Delta\mu_{\text{Si}}$	$p - n \text{ (cm}^{-3}\text{)}$
Bi, Bi ₄ O ₁₂ Si ₃ , Bi ₂ Se ₃ , O ₂ Si	0.0	-0.491	-2.177	-0.252	-5.116	3.02×10^{19}
Bi, Bi ₄ O ₁₂ Si ₃ , Bi ₂ O ₂ Se, Bi ₂ Se ₃	0.0	-0.582	-2.087	-0.252	-5.477	5.39×10^{19}
Bi, Cu ₂ O, Bi ₄ O ₁₂ Si ₃ , Bi ₂ O ₃	0.0	-0.244	-2.012	-0.664	-5.777	5.61×10^{18}
Bi, Bi ₄ O ₁₂ Si ₃ , Bi ₂ O ₂ Se, Bi ₂ O ₃	0.0	-0.507	-2.012	-0.402	-5.777	3.45×10^{19}
Bi, Cu ₂ Se, Cu ₂ O, Bi ₄ O ₁₂ Si ₃	0.0	-0.223	-2.054	-0.643	-5.608	5.11×10^{18}
Bi, Cu ₃ Se ₂ , Bi ₂ Se ₃ , O ₂ Si	0.0	-0.452	-2.216	-0.252	-5.038	2.34×10^{19}
Bi, Bi ₄ O ₁₂ Si ₃ , Cu ₃ Se ₂ , O ₂ Si	0.0	-0.374	-2.177	-0.369	-5.116	1.55×10^{19}
Bi, Cu ₂ Se, Bi ₄ O ₁₂ Si ₃ , Cu ₃ Se ₂	0.0	-0.318	-2.149	-0.453	-5.228	1.1×10^{19}
Bi ₄ O ₁₂ Si ₃ , Cu ₃ Se ₂ , Bi ₂ Se ₃ , O ₂ Si	-0.352	-0.609	-1.942	-0.017	-5.586	6.87×10^{19}
Cu ₂ Se, Cu ₂ O, Bi ₄ O ₁₂ Si ₃ , Cu ₃ Se ₂	-0.285	-0.318	-1.864	-0.453	-5.988	1.13×10^{19}
Cu ₂ O, Bi ₄ O ₁₂ Si ₃ , Cu ₃ Se ₂ , Bi ₂ O ₃	-0.603	-0.445	-1.61	-0.262	-6.581	2.61×10^{19}
Se, Bi ₄ O ₁₂ Si ₃ , Cu ₃ Se ₂ , Bi ₂ O ₃	-0.865	-0.62	-1.435	0.0	-6.931	7.5×10^{19}
Se, Bi ₄ O ₁₂ Si ₃ , Cu ₃ Se ₂ , Bi ₂ Se ₃	-0.378	-0.62	-1.923	0.0	-5.63	7.36×10^{19}
Se, Bi ₄ O ₁₂ Si ₃ , Bi ₂ O ₂ Se, Bi ₂ Se ₃	-0.378	-0.708	-1.835	0.0	-5.981	1.25×10^{20}
Se, Bi ₄ O ₁₂ Si ₃ , Bi ₂ O ₂ Se, Bi ₂ O ₃	-0.603	-0.708	-1.61	0.0	-6.581	1.26×10^{20}

Table S14: Chemical potentials $\Delta\mu_i$ (in eV) in all phase regions of the quinary Bi-Cu-Se-O-Si phase space that are in equilibrium with BiCuSeO. The corresponding charge carrier concentration in each phase region, as determined by charge neutrality at the typical synthesis temperature of 973 K, is listed.

Phase Equilibria of Ge-Doped BiCuSeO

Equilibrium Phases	$\Delta\mu_{\text{Bi}}$	$\Delta\mu_{\text{Cu}}$	$\Delta\mu_{\text{Ge}}$	$\Delta\mu_{\text{O}}$	$\Delta\mu_{\text{Se}}$	$p - n \text{ (cm}^{-3}\text{)}$
Se, Bi ₄ Ge ₃ O ₁₂ , Cu ₃ Se ₂ , Bi ₂ Se ₃	-0.378	-0.62	-2.165	-1.923	0.0	7.36×10^{19}
Se, Bi ₁₂ GeO ₂₀ , Bi ₂ O ₂ Se, Bi ₄ Ge ₃ O ₁₂	-0.582	-0.708	-3.061	-1.63	0.0	1.26×10^{20}
Se, Bi ₁₂ GeO ₂₀ , Bi ₂ O ₂ Se, Bi ₂ O ₃	-0.603	-0.708	-3.224	-1.61	0.0	1.26×10^{20}
Se, Bi ₂ O ₂ Se, Bi ₄ Ge ₃ O ₁₂ , Bi ₂ Se ₃	-0.378	-0.708	-2.515	-1.835	0.0	1.25×10^{20}
Se, Bi ₁₂ GeO ₂₀ , Cu ₃ Se ₂ , Bi ₂ O ₃	-0.865	-0.62	-3.574	-1.435	0.0	7.5×10^{19}
Se, Bi ₁₂ GeO ₂₀ , Bi ₄ Ge ₃ O ₁₂ , Cu ₃ Se ₂	-0.845	-0.62	-3.411	-1.455	0.0	7.48×10^{19}
Bi, Bi ₂ O ₂ Se, Bi ₄ Ge ₃ O ₁₂ , Bi ₂ Se ₃	0.0	-0.582	-2.012	-2.087	-0.252	5.39×10^{19}
Bi, Bi ₁₂ GeO ₂₀ , Bi ₂ O ₂ Se, Bi ₂ O ₃	0.0	-0.507	-2.421	-2.012	-0.402	3.45×10^{19}
Bi, Bi ₁₂ GeO ₂₀ , Bi ₂ O ₂ Se, Bi ₄ Ge ₃ O ₁₂	0.0	-0.514	-2.284	-2.018	-0.388	3.62×10^{19}
Bi, Bi ₄ Ge ₃ O ₁₂ , Cu ₃ Se ₂ , Bi ₂ Se ₃	0.0	-0.452	-1.494	-2.216	-0.252	2.34×10^{19}
Bi, Cu ₂ Se, Bi ₄ Ge ₃ O ₁₂ , Cu ₃ Se ₂	0.0	-0.318	-1.762	-2.149	-0.453	1.1×10^{19}
Bi, Cu ₂ Se, Cu ₂ O, Bi ₄ Ge ₃ O ₁₂	0.0	-0.223	-2.142	-2.054	-0.643	5.11×10^{18}
Bi, Bi ₁₂ GeO ₂₀ , Cu ₂ O, Bi ₂ O ₃	0.0	-0.244	-2.421	-2.012	-0.664	5.61×10^{18}
Bi, Bi ₁₂ GeO ₂₀ , Cu ₂ O, Bi ₄ Ge ₃ O ₁₂	0.0	-0.241	-2.284	-2.018	-0.661	5.54×10^{18}
Cu ₂ Se, Cu ₂ O, Bi ₄ Ge ₃ O ₁₂ , Cu ₃ Se ₂	-0.285	-0.318	-2.522	-1.864	-0.453	1.13×10^{19}
Bi ₁₂ GeO ₂₀ , Cu ₂ O, Cu ₃ Se ₂ , Bi ₂ O ₃	-0.603	-0.445	-3.224	-1.61	-0.262	2.61×10^{19}
Bi ₁₂ GeO ₂₀ , Cu ₂ O, Bi ₄ Ge ₃ O ₁₂ , Cu ₃ Se ₂	-0.552	-0.425	-3.02	-1.651	-0.293	2.3×10^{19}

Table S15: Chemical potentials $\Delta\mu_i$ (in eV) in all phase regions of the quinary Bi-Cu-Se-O-Ge phase space that are in equilibrium with BiCuSeO. The corresponding charge carrier concentration in each phase region, as determined by charge neutrality at the typical synthesis temperature of 973 K, is listed.

Phase Equilibria of Sn-Doped BiCuSeO

Equilibrium Phases	$\Delta\mu_{\text{Bi}}$	$\Delta\mu_{\text{Cu}}$	$\Delta\mu_{\text{O}}$	$\Delta\mu_{\text{Se}}$	$\Delta\mu_{\text{Sn}}$	$p - n \text{ (cm}^{-3}\text{)}$
Se, O ₂ Sn, Cu ₃ Se ₂ , Bi ₂ Se ₃	-0.378	-0.62	-1.923	0.0	-1.897	7.36×10^{19}
Se, Bi ₂ O ₂ Se, Bi ₂ O ₇ Sn ₂ , Bi ₂ O ₃	-0.603	-0.708	-1.61	0.0	-2.676	1.26×10^{20}
Se, Bi ₂ O ₂ Se, Bi ₂ O ₇ Sn ₂ , Bi ₂ Se ₃	-0.378	-0.708	-1.835	0.0	-2.113	1.25×10^{20}
Se, O ₂ Sn, Bi ₂ O ₇ Sn ₂ , Bi ₂ Se ₃	-0.378	-0.68	-1.863	0.0	-2.017	1.06×10^{20}
Se, O ₂ Sn, Bi ₂ O ₇ Sn ₂ , Cu ₃ Se ₂	-0.557	-0.62	-1.743	0.0	-2.256	7.48×10^{19}
Se, Bi ₂ O ₇ Sn ₂ , Cu ₃ Se ₂ , Bi ₂ O ₃	-0.865	-0.62	-1.435	0.0	-3.026	7.5×10^{19}
Cu ₂ O, Bi ₂ O ₇ Sn ₂ , Cu ₂ Se, Cu ₃ Se ₂	-0.285	-0.318	-1.864	-0.453	-2.104	1.13×10^{19}
O ₂ Sn, Bi ₂ O ₇ Sn ₂ , Cu ₂ Se, Cu ₃ Se ₂	-0.104	-0.318	-2.045	-0.453	-1.652	1.13×10^{19}
Cu ₂ O, Bi ₂ O ₇ Sn ₂ , Cu ₃ Se ₂ , Bi ₂ O ₃	-0.603	-0.445	-1.61	-0.262	-2.676	2.61×10^{19}
Bi, Cu ₂ O, Bi ₂ O ₇ Sn ₂ , Bi ₂ O ₃	0.0	-0.244	-2.012	-0.664	-1.873	5.61×10^{18}
Bi, O ₂ Sn, Bi ₂ O ₇ Sn ₂ , Cu ₂ Se	0.0	-0.283	-2.114	-0.522	-1.513	8.61×10^{18}
Bi, Cu ₂ O, Bi ₂ O ₇ Sn ₂ , Cu ₂ Se	0.0	-0.223	-2.054	-0.643	-1.724	5.11×10^{18}
Bi, O ₂ Sn, Cu ₂ Se, Cu ₃ Se ₂	0.0	-0.318	-2.149	-0.453	-1.444	1.11×10^{19}
Bi, O ₂ Sn, Cu ₃ Se ₂ , Bi ₂ Se ₃	0.0	-0.452	-2.216	-0.252	-1.31	2.34×10^{19}
Bi, Bi ₂ O ₂ Se, Bi ₂ O ₇ Sn ₂ , Bi ₂ O ₃	0.0	-0.507	-2.012	-0.402	-1.873	3.45×10^{19}
Bi, Bi ₂ O ₂ Se, Bi ₂ O ₇ Sn ₂ , Bi ₂ Se ₃	0.0	-0.582	-2.087	-0.252	-1.61	5.39×10^{19}
Bi, O ₂ Sn, Bi ₂ O ₇ Sn ₂ , Bi ₂ Se ₃	0.0	-0.554	-2.114	-0.252	-1.513	4.52×10^{19}

Table S16: Chemical potentials $\Delta\mu_i$ (in eV) in all phase regions of the quinary Bi-Cu-Se-O-Sn phase space that are in equilibrium with BiCuSeO. The corresponding charge carrier concentration in each phase region, as determined by charge neutrality at the typical synthesis temperature of 973 K, is listed.

Phase Equilibria of Pb-Doped BiCuSeO

Equilibrium Phases	$\Delta\mu_{\text{Bi}}$	$\Delta\mu_{\text{Cu}}$	$\Delta\mu_{\text{O}}$	$\Delta\mu_{\text{Pb}}$	$\Delta\mu_{\text{Se}}$	$p - n \text{ (cm}^{-3}\text{)}$
Se, PbSe, Cu ₃ Se ₂ , Bi ₂ Se ₃	-0.378	-0.62	-1.923	-0.942	0.0	8.28×10^{19}
Se, PbSe, Bi ₂ O ₂ Se, Bi ₂ O ₃	-0.602	-0.708	-1.61	-0.942	0.0	1.92×10^{20}
Se, PbSe, Bi ₂ O ₂ Se, Bi ₂ Se ₃	-0.378	-0.708	-1.835	-0.942	0.0	1.3×10^{20}
Se, PbSe, Cu ₃ Se ₂ , O ₅ Pb ₃ Se	-0.772	-0.62	-1.528	-0.942	0.0	4×10^{20}
Se, O ₃ PbSe, Cu ₃ Se ₂ , O ₅ Pb ₃ Se	-0.773	-0.62	-1.527	-0.943	0.0	4×10^{20}
Se, O ₃ PbSe, Cu ₃ Se ₂ , Bi ₂ O ₃	-0.865	-0.62	-1.435	-1.22	0.0	1.54×10^{20}
Se, O ₃ PbSe, Bi ₂ O ₃ , O ₅ Pb ₃ Se	-0.727	-0.666	-1.527	-0.943	0.0	3.17×10^{20}
Se, PbSe, Bi ₂ O ₃ , O ₅ Pb ₃ Se	-0.726	-0.667	-1.528	-0.942	0.0	3.17×10^{20}
Bi, PbSe, Bi ₂ O ₂ Se, Bi ₂ Se ₃	0.0	-0.582	-2.087	-0.69	-0.252	5.62×10^{19}
Bi, Cu ₂ Se, Cu ₂ O ₂ Pb, OPb	0.0	-0.228	-2.059	-0.335	-0.632	6.01×10^{19}
Bi, PbSe, Cu ₂ Se, OPb	0.0	-0.237	-2.068	-0.326	-0.616	6.59×10^{19}
Bi, Cu ₂ Se, Cu ₂ O, Cu ₂ O ₂ Pb	0.0	-0.223	-2.054	-0.356	-0.643	5.31×10^{19}
Bi, Cu ₂ O ₂ Pb, Bi ₂ O ₃ , OPb	0.0	-0.252	-2.012	-0.382	-0.656	4.6×10^{19}
Bi, Cu ₂ O, Cu ₂ O ₂ Pb, Bi ₂ O ₃	0.0	-0.244	-2.012	-0.398	-0.664	4.18×10^{19}
Bi, PbSe, Bi ₂ O ₃ , OPb	0.0	-0.349	-2.012	-0.382	-0.56	6.32×10^{19}
Bi, PbSe, Bi ₂ O ₂ Se, Bi ₂ O ₃	0.0	-0.507	-2.012	-0.54	-0.402	5.11×10^{19}
Bi, PbSe, Cu ₃ Se ₂ , Bi ₂ Se ₃	0.0	-0.452	-2.216	-0.69	-0.252	2.74×10^{19}
Bi, PbSe, Cu ₂ Se, Cu ₃ Se ₂	0.0	-0.318	-2.149	-0.489	-0.453	4.58×10^{19}
Cu ₂ O, Cu ₂ O ₂ Pb, Cu ₃ Se ₂ , Bi ₂ O ₃	-0.603	-0.445	-1.61	-0.8	-0.262	2.94×10^{20}
Cu ₂ O ₂ Pb, Cu ₃ Se ₂ , Bi ₂ O ₃ , OPb	-0.627	-0.461	-1.594	-0.8	-0.238	3.42×10^{20}
PbSe, Cu ₃ Se ₂ , O ₅ Pb ₃ Se, OPb	-0.679	-0.536	-1.579	-0.815	-0.127	4.58×10^{20}
Cu ₃ Se ₂ , Bi ₂ O ₃ , O ₅ Pb ₃ Se, OPb	-0.688	-0.502	-1.553	-0.841	-0.178	4.03×10^{20}
O ₃ PbSe, Cu ₃ Se ₂ , Bi ₂ O ₃ , O ₅ Pb ₃ Se	-0.786	-0.567	-1.488	-0.983	-0.079	3.36×10^{20}
PbSe, Bi ₂ O ₃ , O ₅ Pb ₃ Se, OPb	-0.649	-0.565	-1.579	-0.815	-0.127	3.91×10^{20}
PbSe, Cu ₂ Se, Cu ₃ Se ₂ , OPb	-0.244	-0.318	-1.905	-0.489	-0.453	1.56×10^{20}
Cu ₂ Se, Cu ₂ O ₂ Pb, Cu ₃ Se ₂ , OPb	-0.269	-0.318	-1.88	-0.514	-0.453	1.56×10^{20}
Cu ₂ Se, Cu ₂ O, Cu ₂ O ₂ Pb, Cu ₃ Se ₂	-0.285	-0.318	-1.864	-0.546	-0.453	1.46×10^{20}

Table S17: Chemical potentials $\Delta\mu_i$ (in eV) in all phase regions of the quinary Bi-Cu-Se-O-Pb phase space that are in equilibrium with BiCuSeO. The corresponding charge carrier concentration in each phase region, as determined by charge neutrality at the typical synthesis temperature of 973 K, is listed.

Phase Equilibria of Sc-Doped BiCuSeO

Equilibrium Phases	$\Delta\mu_{\text{Bi}}$	$\Delta\mu_{\text{Cu}}$	$\Delta\mu_{\text{O}}$	$\Delta\mu_{\text{Sc}}$	$\Delta\mu_{\text{Se}}$	$p - n \text{ (cm}^{-3}\text{)}$
Se, O_3Sc_2 , Cu_3Se_2 , Bi_2Se_3	-0.378	-0.62	-1.923	-6.969	0.0	7.36×10^{19}
Se, O_3Sc_2 , $\text{Bi}_2\text{O}_2\text{Se}$, Bi_2O_3	-0.602	-0.708	-1.61	-7.437	0.0	1.26×10^{20}
Se, O_3Sc_2 , $\text{Bi}_2\text{O}_2\text{Se}$, Bi_2Se_3	-0.378	-0.708	-1.835	-7.1	0.0	1.25×10^{20}
Se, O_3Sc_2 , Cu_3Se_2 , Bi_2O_3	-0.865	-0.62	-1.435	-7.7	0.0	7.5×10^{19}
Bi, O_3Sc_2 , $\text{Bi}_2\text{O}_2\text{Se}$, Bi_2Se_3	0.0	-0.582	-2.087	-6.723	-0.252	5.39×10^{19}
Bi, Cu_2Se , Cu_2O , CuO_2Sc	0.0	-0.223	-2.054	-6.817	-0.643	5.11×10^{18}
Bi, O_3Sc_2 , Cu_2Se , CuO_2Sc	0.0	-0.253	-2.084	-6.726	-0.582	6.72×10^{18}
Bi, O_3Sc_2 , CuO_2Sc , Bi_2O_3	0.0	-0.29	-2.012	-6.835	-0.619	7.98×10^{18}
Bi, Cu_2O , CuO_2Sc , Bi_2O_3	0.0	-0.244	-2.012	-6.881	-0.664	5.61×10^{18}
Bi, O_3Sc_2 , $\text{Bi}_2\text{O}_2\text{Se}$, Bi_2O_3	0.0	-0.507	-2.012	-6.835	-0.402	3.45×10^{19}
Bi, O_3Sc_2 , Cu_3Se_2 , Bi_2Se_3	0.0	-0.452	-2.216	-6.528	-0.252	2.34×10^{19}
Bi, O_3Sc_2 , Cu_2Se , Cu_3Se_2	0.0	-0.318	-2.149	-6.629	-0.453	1.1×10^{19}
O_3Sc_2 , Cu_2Se , CuO_2Sc , Cu_3Se_2	-0.194	-0.318	-1.955	-6.92	-0.453	1.13×10^{19}
Cu_2Se , Cu_2O , CuO_2Sc , Cu_3Se_2	-0.285	-0.318	-1.864	-7.102	-0.453	1.13×10^{19}
O_3Sc_2 , CuO_2Sc , Cu_3Se_2 , Bi_2O_3	-0.739	-0.536	-1.519	-7.574	-0.126	4.54×10^{19}
Cu_2O , CuO_2Sc , Cu_3Se_2 , Bi_2O_3	-0.603	-0.445	-1.61	-7.483	-0.262	2.61×10^{19}

Table S18: Chemical potentials $\Delta\mu_i$ (in eV) in all phase regions of the quinary Bi-Cu-Se-O-Sc phase space that are in equilibrium with BiCuSeO. The corresponding charge carrier concentration in each phase region, as determined by charge neutrality at the typical synthesis temperature of 973 K, is listed.

Phase Equilibria of Y-Doped BiCuSeO

Equilibrium Phases	$\Delta\mu_{\text{Bi}}$	$\Delta\mu_{\text{Cu}}$	$\Delta\mu_{\text{O}}$	$\Delta\mu_{\text{Se}}$	$\Delta\mu_{\text{Y}}$	$p - n \text{ (cm}^{-3}\text{)}$
Bi, Bi ₂ O ₂ Se, Bi ₂ Se ₃ , O ₃ Y ₂	0.0	-0.582	-2.087	-0.252	-6.748	5.31e+19
Bi, Cu ₂ O, Bi ₂ O ₃ , O ₃ Y ₂	0.0	-0.244	-2.012	-0.664	-6.86	5.59e+18
Bi, Cu ₂ Se, Cu ₂ O, O ₃ Y ₂	0.0	-0.223	-2.054	-0.643	-6.796	5.08e+18
Bi, Bi ₂ O ₂ Se, Bi ₂ O ₃ , O ₃ Y ₂	0.0	-0.507	-2.012	-0.402	-6.86	3.44e+19
Bi, Cu ₃ Se ₂ , Bi ₂ Se ₃ , O ₃ Y ₂	0.0	-0.452	-2.216	-0.252	-6.553	2.04e+19
Bi, Cu ₂ Se, Cu ₃ Se ₂ , O ₃ Y ₂	0.0	-0.318	-2.149	-0.453	-6.654	1.05e+19
Cu ₂ Se, Cu ₂ O, Cu ₃ Se ₂ , O ₃ Y ₂	-0.285	-0.318	-1.864	-0.453	-7.082	1.12e+19
Cu ₂ O, Cu ₃ Se ₂ , Bi ₂ O ₃ , O ₃ Y ₂	-0.603	-0.445	-1.61	-0.262	-7.463	2.59e+19
Se, Cu ₃ Se ₂ , Bi ₂ O ₃ , O ₃ Y ₂	-0.865	-0.62	-1.435	0.0	-7.725	7.46e+19
Se, Bi ₂ O ₂ Se, Bi ₂ Se ₃ , O ₃ Y ₂	-0.378	-0.708	-1.835	0.0	-7.125	1.22e+20
Se, Bi ₂ O ₂ Se, Bi ₂ O ₃ , O ₃ Y ₂	-0.602	-0.708	-1.61	0.0	-7.462	1.25e+20
Se, Cu ₃ Se ₂ , Bi ₂ Se ₃ , O ₃ Y ₂	-0.378	-0.62	-1.923	0.0	-6.994	6.67e+19

Table S19: Chemical potentials $\Delta\mu_i$ (in eV) in all phase regions of the quinary Bi-Cu-Se-O-Y phase space that are in equilibrium with BiCuSeO. The corresponding charge carrier concentration in each phase region, as determined by charge neutrality at the typical synthesis temperature of 973 K, is listed.

Phase Equilibria of Ti-Doped BiCuSeO

Equilibrium Phases	$\Delta\mu_{\text{Bi}}$	$\Delta\mu_{\text{Cu}}$	$\Delta\mu_{\text{O}}$	$\Delta\mu_{\text{Se}}$	$\Delta\mu_{\text{Ti}}$	$p - n \text{ (cm}^{-3}\text{)}$
Bi, Bi ₂ O ₂ Se, Bi ₂ O ₇ Ti ₂ , Bi ₂ Se ₃	0.0	-0.582	-2.087	-0.252	-5.733	5.39×10^{19}
Bi, Bi ₂ O ₇ Ti ₂ , O ₂ Ti, Bi ₂ Se ₃	0.0	-0.567	-2.101	-0.252	-5.683	4.91×10^{19}
Bi, Bi ₂ O ₂ Se, Bi ₂ O ₇ Ti ₂ , Bi ₂ O ₃	0.0	-0.507	-2.012	-0.402	-5.996	3.45×10^{19}
Bi, Cu ₂ Se, Cu ₂ O, Bi ₂ O ₇ Ti ₂	0.0	-0.223	-2.054	-0.643	-5.847	5.11×10^{18}
Bi, Cu ₂ Se, Bi ₂ O ₇ Ti ₂ , O ₂ Ti	0.0	-0.27	-2.101	-0.549	-5.683	7.74×10^{18}
Bi, Cu ₂ O, Bi ₂ O ₇ Ti ₂ , Bi ₂ O ₃	0.0	-0.244	-2.012	-0.664	-5.996	5.61×10^{18}
Bi, Cu ₃ Se ₂ , O ₂ Ti, Bi ₂ Se ₃	0.0	-0.452	-2.216	-0.252	-5.453	2.34×10^{19}
Bi, Cu ₂ Se, Cu ₃ Se ₂ , O ₂ Ti	0.0	-0.318	-2.149	-0.453	-5.587	1.1×10^{19}
Cu ₂ Se, Cu ₂ O, Bi ₂ O ₇ Ti ₂ , Cu ₃ Se ₂	-0.285	-0.318	-1.864	-0.453	-6.227	1.13×10^{19}
Cu ₂ Se, Bi ₂ O ₇ Ti ₂ , Cu ₃ Se ₂ , O ₂ Ti	-0.144	-0.318	-2.005	-0.453	-5.875	1.13×10^{19}
Cu ₂ O, Bi ₂ O ₇ Ti ₂ , Cu ₃ Se ₂ , Bi ₂ O ₃	-0.603	-0.445	-1.61	-0.262	-6.799	2.61×10^{19}
Se, Bi ₂ O ₇ Ti ₂ , Cu ₃ Se ₂ , Bi ₂ O ₃	-0.865	-0.62	-1.435	0.0	-7.149	7.5×10^{19}
Se, Bi ₂ O ₇ Ti ₂ , Cu ₃ Se ₂ , O ₂ Ti	-0.597	-0.62	-1.703	0.0	-6.479	7.48×10^{19}
Se, Bi ₂ O ₂ Se, Bi ₂ O ₇ Ti ₂ , Bi ₂ Se ₃	-0.378	-0.708	-1.835	0.0	-6.237	1.25×10^{20}
Se, Bi ₂ O ₇ Ti ₂ , O ₂ Ti, Bi ₂ Se ₃	-0.378	-0.693	-1.849	0.0	-6.186	1.14×10^{20}
Se, Bi ₂ O ₂ Se, Bi ₂ O ₇ Ti ₂ , Bi ₂ O ₃	-0.602	-0.708	-1.61	0.0	-6.799	1.26×10^{20}
Se, Cu ₃ Se ₂ , O ₂ Ti, Bi ₂ Se ₃	-0.378	-0.62	-1.923	0.0	-6.04	7.36×10^{19}

Table S20: Chemical potentials $\Delta\mu_i$ (in eV) in all phase regions of the quinary Bi-Cu-Se-O-Ti phase space that are in equilibrium with BiCuSeO. The corresponding charge carrier concentration in each phase region, as determined by charge neutrality at the typical synthesis temperature of 973 K, is listed.

Phase Equilibria of Zr-Doped BiCuSeO

Equilibrium Phases	$\Delta\mu_{\text{Bi}}$	$\Delta\mu_{\text{Cu}}$	$\Delta\mu_{\text{O}}$	$\Delta\mu_{\text{Se}}$	$\Delta\mu_{\text{Zr}}$	$p - n \text{ (cm}^{-3}\text{)}$
Bi, Bi ₂ O ₂ Se, O ₂ Zr, Bi ₂ Se ₃	0.0	-0.582	-2.087	-0.252	-7.229	5.39×10^{19}
Bi, Cu ₂ Se, Cu ₂ O, O ₂ Zr	0.0	-0.223	-2.054	-0.643	-7.294	5.11×10^{18}
Bi, Cu ₂ O, O ₂ Zr, Bi ₂ O ₃	0.0	-0.244	-2.012	-0.664	-7.379	5.61×10^{18}
Bi, Bi ₂ O ₂ Se, O ₂ Zr, Bi ₂ O ₃	0.0	-0.507	-2.012	-0.402	-7.379	3.45×10^{19}
Bi, O ₂ Zr, Cu ₃ Se ₂ , Bi ₂ Se ₃	0.0	-0.452	-2.216	-0.252	-6.97	2.34×10^{19}
Bi, Cu ₂ Se, O ₂ Zr, Cu ₃ Se ₂	0.0	-0.318	-2.149	-0.453	-7.104	1.1×10^{19}
Cu ₂ O, O ₂ Zr, Cu ₃ Se ₂ , Bi ₂ O ₃	-0.603	-0.445	-1.61	-0.262	-8.182	2.61×10^{19}
Cu ₂ Se, Cu ₂ O, O ₂ Zr, Cu ₃ Se ₂	-0.285	-0.318	-1.864	-0.453	-7.674	1.13×10^{19}
Se, O ₂ Zr, Cu ₃ Se ₂ , Bi ₂ O ₃	-0.865	-0.62	-1.435	0.0	-8.532	7.5×10^{19}
Se, Bi ₂ O ₂ Se, O ₂ Zr, Bi ₂ Se ₃	-0.378	-0.708	-1.835	0.0	-7.732	1.25×10^{20}
Se, Bi ₂ O ₂ Se, O ₂ Zr, Bi ₂ O ₃	-0.602	-0.708	-1.61	0.0	-8.182	1.26×10^{20}
Se, O ₂ Zr, Cu ₃ Se ₂ , Bi ₂ Se ₃	-0.378	-0.62	-1.923	0.0	-7.557	7.36×10^{19}

Table S21: Chemical potentials $\Delta\mu_i$ (in eV) in all phase regions of the quinary Bi-Cu-Se-O-Zr phase space that are in equilibrium with BiCuSeO. The corresponding charge carrier concentration in each phase region, as determined by charge neutrality at the typical synthesis temperature of 973 K, is listed.

Phase Equilibria of Hf-Doped BiCuSeO

Equilibrium Phases	$\Delta\mu_{\text{Bi}}$	$\Delta\mu_{\text{Cu}}$	$\Delta\mu_{\text{Hf}}$	$\Delta\mu_{\text{O}}$	$\Delta\mu_{\text{Se}}$	$p - n \text{ (cm}^{-3}\text{)}$
Se, HfO ₂ , Cu ₃ Se ₂ , Bi ₂ Se ₃	-0.378	-0.62	-8.0	-1.923	0.0	7.36×10^{19}
Se, Bi ₂ O ₂ Se, HfO ₂ , Bi ₈ Hf ₈ O ₂₈	-0.517	-0.708	-8.454	-1.695	0.0	1.25×10^{20}
Se, Bi ₂ O ₂ Se, Bi ₂ O ₃ , Bi ₈ Hf ₈ O ₂₈	-0.603	-0.708	-8.668	-1.61	0.0	1.26×10^{20}
Se, Bi ₂ O ₂ Se, HfO ₂ , Bi ₂ Se ₃	-0.378	-0.708	-8.175	-1.835	0.0	1.25×10^{20}
Se, HfO ₂ , Cu ₃ Se ₂ , Bi ₈ Hf ₈ O ₂₈	-0.78	-0.62	-8.805	-1.52	0.0	7.48×10^{19}
Se, Cu ₃ Se ₂ , Bi ₂ O ₃ , Bi ₈ Hf ₈ O ₂₈	-0.865	-0.62	-9.018	-1.435	0.0	7.48×10^{19}
Bi, Bi ₂ O ₂ Se, HfO ₂ , Bi ₂ Se ₃	0.0	-0.582	-7.672	-2.087	-0.252	5.4×10^{19}
Bi, Cu ₂ Se, Cu ₂ O, HfO ₂	0.0	-0.223	-7.737	-2.054	-0.643	5.11×10^{18}
Bi, Cu ₂ O, HfO ₂ , Bi ₈ Hf ₈ O ₂₈	0.0	-0.23	-7.765	-2.04	-0.65	5.29×10^{18}
Bi, Cu ₂ O, Bi ₂ O ₃ , Bi ₈ Hf ₈ O ₂₈	0.0	-0.244	-7.864	-2.012	-0.664	5.61×10^{18}
Bi, Bi ₂ O ₂ Se, Bi ₂ O ₃ , Bi ₈ Hf ₈ O ₂₈	0.0	-0.507	-7.864	-2.012	-0.402	3.44×10^{19}
Bi, Bi ₂ O ₂ Se, HfO ₂ , Bi ₈ Hf ₈ O ₂₈	0.0	-0.535	-7.765	-2.04	-0.345	4.14×10^{19}
Bi, HfO ₂ , Cu ₃ Se ₂ , Bi ₂ Se ₃	0.0	-0.452	-7.413	-2.216	-0.252	2.33×10^{19}
Bi, Cu ₂ Se, HfO ₂ , Cu ₃ Se ₂	0.0	-0.318	-7.547	-2.149	-0.453	1.1×10^{19}
Cu ₂ O, Cu ₃ Se ₂ , Bi ₂ O ₃ , Bi ₈ Hf ₈ O ₂₈	-0.603	-0.445	-8.668	-1.61	-0.262	2.6×10^{19}
Cu ₂ O, HfO ₂ , Cu ₃ Se ₂ , Bi ₈ Hf ₈ O ₂₈	-0.39	-0.36	-8.284	-1.78	-0.39	1.51×10^{19}
Cu ₂ Se, Cu ₂ O, HfO ₂ , Cu ₃ Se ₂	-0.285	-0.318	-8.117	-1.864	-0.453	1.13×10^{19}

Table S22: Chemical potentials $\Delta\mu_i$ (in eV) in all phase regions of the quinary Bi-Cu-Se-O-Hf phase space that are in equilibrium with BiCuSeO. The corresponding charge carrier concentration in each phase region, as determined by charge neutrality at the typical synthesis temperature of 973 K, is listed.

Phase Equilibria of F-Doped BiCuSeO

Equilibrium Phases	$\Delta\mu_{\text{Bi}}$	$\Delta\mu_{\text{Cu}}$	$\Delta\mu_{\text{F}}$	$\Delta\mu_{\text{O}}$	$\Delta\mu_{\text{Se}}$	$p - n \text{ (cm}^{-3}\text{)}$
Cu ₂ O, Cu ₃ Se ₂ , Bi ₂ O ₃ , BiFO	-0.632	-0.465	-3.449	-1.601	-0.25	2.62×10^{19}
Cu ₃ Se ₂ , Bi ₇ F ₁₁ O ₅ , Cu ₂ Se, BiFO	-0.263	-0.349	-3.507	-1.913	-0.423	8.12×10^{18}
Cu ₂ O, Cu ₃ Se ₂ , Cu ₂ Se, BiFO	-0.343	-0.349	-3.507	-1.832	-0.423	9.53×10^{18}
Bi, Cu ₃ Se ₂ , Bi ₇ F ₁₁ O ₅ , Cu ₂ Se	0.0	-0.349	-3.555	-2.176	-0.423	2.99×10^{18}
Bi, Cu ₃ Se ₂ , Bi ₇ F ₁₁ O ₅ , Bi ₂ Se ₃	0.0	-0.46	-3.53	-2.231	-0.256	3.82×10^{18}
Bi, Bi ₇ F ₁₁ O ₅ , Bi ₂ O ₂ Se, BiFO	0.0	-0.583	-3.595	-2.088	-0.277	2.61×10^{19}
Bi, Bi ₂ O ₃ , Bi ₂ O ₂ Se, BiFO	0.0	-0.518	-3.66	-2.023	-0.408	2.77×10^{19}
Bi, Bi ₇ F ₁₁ O ₅ , Cu ₂ Se, BiFO	0.0	-0.262	-3.595	-2.088	-0.598	2.93×10^{18}
Bi, Cu ₂ O, Cu ₂ Se, BiFO	0.0	-0.235	-3.621	-2.061	-0.652	2.61×10^{18}
Bi, Cu ₂ O, Bi ₂ O ₃ , BiFO	0.0	-0.254	-3.66	-2.023	-0.671	3.59×10^{18}
Bi, Bi ₇ F ₁₁ O ₅ , Bi ₂ O ₂ Se, Bi ₂ Se ₃	0.0	-0.593	-3.59	-2.098	-0.256	2.59×10^{19}
Se, Cu ₃ Se ₂ , Bi ₇ F ₁₁ O ₅ , BiFO	-0.686	-0.631	-3.366	-1.631	0.0	7×10^{19}
Se, Cu ₃ Se ₂ , Bi ₂ O ₃ , BiFO	-0.882	-0.631	-3.366	-1.435	0.0	7.77×10^{19}
Se, Bi ₇ F ₁₁ O ₅ , Bi ₂ O ₂ Se, Bi ₂ Se ₃	-0.385	-0.722	-3.462	-1.842	0.0	9.44×10^{19}
Se, Bi ₂ O ₃ , Bi ₂ O ₂ Se, BiFO	-0.611	-0.722	-3.456	-1.615	0.0	1.31×10^{20}
Se, Bi ₇ F ₁₁ O ₅ , Bi ₂ O ₂ Se, BiFO	-0.415	-0.722	-3.456	-1.811	0.0	1.01×10^{20}
Se, Cu ₃ Se ₂ , Bi ₇ F ₁₁ O ₅ , Bi ₂ Se ₃	-0.385	-0.631	-3.421	-1.932	0.0	3.23×10^{19}

Table S23: Chemical potentials $\Delta\mu_i$ (in eV) in all phase regions of the quinary Bi-Cu-Se-O-F phase space that are in equilibrium with BiCuSeO. The corresponding charge carrier concentration in each phase region, as determined by charge neutrality at the typical synthesis temperature of 973 K, is listed.

Phase Equilibria of Cl-Doped BiCuSeO

Equilibrium Phases	$\Delta\mu_{\text{Bi}}$	$\Delta\mu_{\text{Cl}}$	$\Delta\mu_{\text{Cu}}$	$\Delta\mu_{\text{O}}$	$\Delta\mu_{\text{Se}}$	$p - n \text{ (cm}^{-3}\text{)}$
Se, BiClO, Cu ₃ Se ₂ , Bi ₂ Se ₃	-0.378	-1.43	-0.62	-1.923	0.0	3.32×10^{19}
Se, Bi ₂ O ₂ Se, Bi ₂ O ₃ , Bi ₄₈ Cl ₂₀ O ₆₂	-0.603	-1.627	-0.708	-1.61	0.0	1.05×10^{20}
Se, BiClO, Bi ₂ O ₂ Se, Bi ₄₈ Cl ₂₀ O ₆₂	-0.446	-1.518	-0.708	-1.767	0.0	7.95×10^{19}
Se, BiClO, Bi ₂ O ₂ Se, Bi ₂ Se ₃	-0.378	-1.518	-0.708	-1.835	0.0	7.92×10^{19}
Se, BiClO, Cu ₃ Se ₂ , Bi ₄₈ Cl ₂₀ O ₆₂	-0.708	-1.43	-0.62	-1.592	0.0	3.34×10^{19}
Se, Cu ₃ Se ₂ , Bi ₂ O ₃ , Bi ₄₈ Cl ₂₀ O ₆₂	-0.865	-1.54	-0.62	-1.435	0.0	5.15×10^{19}
Bi, BiClO, Bi ₂ O ₂ Se, Bi ₂ Se ₃	0.0	-1.643	-0.582	-2.087	-0.252	2.18×10^{19}
Bi, BiClO, Bi ₂ O ₂ Se, Bi ₄₈ Cl ₂₀ O ₆₂	0.0	-1.666	-0.559	-2.064	-0.297	1.71×10^{19}
Bi, Bi ₂ O ₂ Se, Bi ₂ O ₃ , Bi ₄₈ Cl ₂₀ O ₆₂	0.0	-1.828	-0.507	-2.012	-0.402	1.66×10^{19}
Bi, Cu ₂ Se, Cu ₂ O, Bi ₄₈ Cl ₂₀ O ₆₂	0.0	-1.697	-0.223	-2.054	-0.643	-2.32×10^{18}
Bi, Cu ₂ Se, BiClO, Bi ₄₈ Cl ₂₀ O ₆₂	0.0	-1.666	-0.233	-2.064	-0.623	-2.35×10^{18}
Bi, Cu ₂ O, Bi ₂ O ₃ , Bi ₄₈ Cl ₂₀ O ₆₂	0.0	-1.828	-0.244	-2.012	-0.664	-4.58×10^{17}
Bi, BiClO, Cu ₃ Se ₂ , Bi ₂ Se ₃	0.0	-1.514	-0.452	-2.216	-0.252	4.83×10^{18}
Bi, Cu ₂ Se, BiClO, Cu ₃ Se ₂	0.0	-1.581	-0.318	-2.149	-0.453	9.94×10^{14}
Cu ₂ O, Cu ₃ Se ₂ , Bi ₂ O ₃ , Bi ₄₈ Cl ₂₀ O ₆₂	-0.603	-1.627	-0.445	-1.61	-0.262	8.51×10^{18}
Cu ₂ Se, BiClO, Cu ₃ Se ₂ , Bi ₄₈ Cl ₂₀ O ₆₂	-0.255	-1.581	-0.318	-1.894	-0.453	3.5×10^{16}
Cu ₂ Se, Cu ₂ O, Cu ₃ Se ₂ , Bi ₄₈ Cl ₂₀ O ₆₂	-0.285	-1.602	-0.318	-1.864	-0.453	3.02×10^{17}

Table S24: Chemical potentials $\Delta\mu_i$ (in eV) in all phase regions of the quinary Bi-Cu-Se-O-Cl phase space that are in equilibrium with BiCuSeO. The corresponding charge carrier concentration in each phase region, as determined by charge neutrality at the typical synthesis temperature of 973 K, is listed.

Phase Equilibria of Br-Doped BiCuSeO

Equilibrium Phases	$\Delta\mu_{\text{Bi}}$	$\Delta\mu_{\text{Br}}$	$\Delta\mu_{\text{Cu}}$	$\Delta\mu_{\text{O}}$	$\Delta\mu_{\text{Se}}$	$p - n \text{ (cm}^{-3}\text{)}$
Bi ₄ Br ₂ O ₅ , Cu ₂ O, Cu ₃ Se ₂ , Bi ₂ O ₃	-0.603	-1.082	-0.445	-1.61	-0.262	1.02×10^{19}
Bi ₄ Br ₂ O ₅ , Cu ₃ Se ₂ , Bi ₂ O ₃ , Bi ₆ Br ₂ O ₁₄ Se ₃	-0.833	-1.006	-0.599	-1.456	-0.032	4.75×10^{19}
Bi ₄ Br ₂ O ₅ , Cu ₂ Se, Cu ₃ Se ₂ , BiBrO	-0.152	-1.016	-0.318	-1.997	-0.453	2.06×10^{17}
Bi ₄ Br ₂ O ₅ , Cu ₂ O, Cu ₂ Se, Cu ₃ Se ₂	-0.285	-1.082	-0.318	-1.864	-0.453	1.07×10^{18}
Bi, Cu ₂ Se, Cu ₃ Se ₂ , BiBrO	0.0	-1.016	-0.318	-2.149	-0.453	1.92×10^{17}
Bi, Cu ₃ Se ₂ , BiBrO, Bi ₂ Se ₃	0.0	-0.949	-0.452	-2.216	-0.252	5.31×10^{18}
Bi, Bi ₄ Br ₂ O ₅ , Bi ₂ O ₂ Se, Bi ₂ O ₃	0.0	-1.283	-0.507	-2.012	-0.402	1.94×10^{19}
Bi, Bi ₄ Br ₂ O ₅ , Bi ₂ O ₂ Se, Bi ₂ Se ₃	0.0	-1.096	-0.582	-2.087	-0.252	2.57×10^{19}
Bi, Bi ₄ Br ₂ O ₅ , BiBrO, Bi ₂ Se ₃	0.0	-1.067	-0.57	-2.098	-0.252	2.08×10^{19}
Bi, Bi ₄ Br ₂ O ₅ , Cu ₂ O, Bi ₂ O ₃	0.0	-1.283	-0.244	-2.012	-0.664	-2.62×10^{16}
Bi, Bi ₄ Br ₂ O ₅ , Cu ₂ O, Cu ₂ Se	0.0	-1.177	-0.223	-2.054	-0.643	-1.37×10^{18}
Bi, Bi ₄ Br ₂ O ₅ , Cu ₂ Se, BiBrO	0.0	-1.067	-0.267	-2.098	-0.554	-1.07×10^{18}
Se, Bi ₄ Br ₂ O ₅ , Bi ₂ O ₃ , Bi ₆ Br ₂ O ₁₄ Se ₃	-0.809	-1.014	-0.639	-1.472	0.0	6.63×10^{19}
Se, Cu ₃ Se ₂ , Bi ₂ O ₃ , Bi ₆ Br ₂ O ₁₄ Se ₃	-0.865	-1.108	-0.62	-1.435	0.0	6.84×10^{19}
Se, Bi ₄ Br ₂ O ₅ , Cu ₃ Se ₂ , BiBrO	-0.605	-0.865	-0.62	-1.695	0.0	3.58×10^{19}
Se, Bi ₄ Br ₂ O ₅ , Cu ₃ Se ₂ , Bi ₆ Br ₂ O ₁₄ Se ₃	-0.833	-0.979	-0.62	-1.467	0.0	5.45×10^{19}
Se, Bi ₄ Br ₂ O ₅ , BiBrO, Bi ₂ Se ₃	-0.378	-0.941	-0.696	-1.847	0.0	7.51×10^{19}
Se, Bi ₄ Br ₂ O ₅ , Bi ₂ O ₂ Se, Bi ₂ Se ₃	-0.378	-0.97	-0.708	-1.835	0.0	8.8×10^{19}
Se, Bi ₄ Br ₂ O ₅ , Bi ₂ O ₂ Se, Bi ₂ O ₃	-0.603	-1.083	-0.708	-1.61	0.0	1.11×10^{20}
Se, Cu ₃ Se ₂ , BiBrO, Bi ₂ Se ₃	-0.378	-0.865	-0.62	-1.923	0.0	3.57×10^{19}

Table S25: Chemical potentials $\Delta\mu_i$ (in eV) in all phase regions of the quinary Bi-Cu-Se-O-Br phase space that are in equilibrium with BiCuSeO. The corresponding charge carrier concentration in each phase region, as determined by charge neutrality at the typical synthesis temperature of 973 K, is listed.

Phase Equilibria of I-Doped BiCuSeO

Equilibrium Phases	$\Delta\mu_{\text{Bi}}$	$\Delta\mu_{\text{Cu}}$	$\Delta\mu_{\text{I}}$	$\Delta\mu_{\text{O}}$	$\Delta\mu_{\text{Se}}$	$p - n \text{ (cm}^{-3}\text{)}$
Se, Bi ₄ I ₂ O ₅ , Bi ₂ O ₂ Se, Bi ₂ O ₃	-0.602	-0.708	-0.547	-1.61	0.0	1.24×10^{20}
Se, Bi ₄ I ₂ O ₅ , Bi ₂ O ₂ Se, Bi ₂ Se ₃	-0.378	-0.708	-0.435	-1.835	0.0	1.18×10^{20}
Se, BiIO, Bi ₄ I ₂ O ₅ , Bi ₂ Se ₃	-0.378	-0.685	-0.379	-1.857	0.0	9.84×10^{19}
Se, BiIO, Cu ₃ Se ₂ , Bi ₂ Se ₃	-0.378	-0.62	-0.314	-1.923	0.0	6.1×10^{19}
Se, BiIO, Bi ₄ I ₂ O ₅ , Cu ₃ Se ₂	-0.573	-0.62	-0.314	-1.727	0.0	6.16×10^{19}
Se, Bi ₄ I ₂ O ₅ , Cu ₃ Se ₂ , Bi ₂ O ₃	-0.865	-0.62	-0.46	-1.435	0.0	7.2×10^{19}
Bi, BiIO, CuI, Bi ₂ Se ₃	0.0	-0.455	-0.401	-2.213	-0.252	1.33×10^{19}
Bi, BiIO, Bi ₄ I ₂ O ₅ , Bi ₂ Se ₃	0.0	-0.559	-0.505	-2.109	-0.252	3.57×10^{19}
Bi, Bi ₄ I ₂ O ₅ , Bi ₂ O ₂ Se, Bi ₂ Se ₃	0.0	-0.582	-0.561	-2.087	-0.252	4.6×10^{19}
Bi, Cu ₂ O, Bi ₄ I ₂ O ₅ , Bi ₂ O ₃	0.0	-0.244	-0.748	-2.012	-0.664	2.41×10^{18}
Bi, Bi ₄ I ₂ O ₅ , Bi ₂ O ₂ Se, Bi ₂ O ₃	0.0	-0.507	-0.748	-2.012	-0.402	3.1×10^{19}
Bi, BiIO, Bi ₄ I ₂ O ₅ , CuI	0.0	-0.351	-0.505	-2.109	-0.46	4.14×10^{18}
Bi, Cu ₂ Se, Cu ₂ O, Bi ₄ I ₂ O ₅	0.0	-0.223	-0.642	-2.054	-0.643	9.13×10^{17}
Bi, Cu ₂ Se, Bi ₄ I ₂ O ₅ , CuI	0.0	-0.229	-0.627	-2.06	-0.63	9.66×10^{17}
Bi, Cu ₃ Se ₂ , CuI, Bi ₂ Se ₃	0.0	-0.452	-0.404	-2.216	-0.252	1.32×10^{19}
Bi, Cu ₂ Se, Cu ₃ Se ₂ , CuI	0.0	-0.318	-0.538	-2.149	-0.453	4.2×10^{18}
BiIO, Cu ₃ Se ₂ , CuI, Bi ₂ Se ₃	-0.027	-0.464	-0.392	-2.195	-0.234	1.47×10^{19}
BiIO, Bi ₄ I ₂ O ₅ , Cu ₃ Se ₂ , CuI	-0.339	-0.464	-0.392	-1.883	-0.234	1.5×10^{19}
Cu ₂ O, Bi ₄ I ₂ O ₅ , Cu ₃ Se ₂ , Bi ₂ O ₃	-0.603	-0.445	-0.547	-1.61	-0.262	2.05×10^{19}
Cu ₂ Se, Cu ₂ O, Bi ₄ I ₂ O ₅ , Cu ₃ Se ₂	-0.285	-0.318	-0.547	-1.864	-0.453	4.45×10^{18}
Cu ₂ Se, Bi ₄ I ₂ O ₅ , Cu ₃ Se ₂ , CuI	-0.266	-0.318	-0.538	-1.883	-0.453	4.22×10^{18}

Table S26: Chemical potentials $\Delta\mu_i$ (in eV) in all phase regions of the quinary Bi-Cu-Se-O-I phase space that are in equilibrium with BiCuSeO. The corresponding charge carrier concentration in each phase region, as determined by charge neutrality at the typical synthesis temperature of 973 K, is listed.

References

- (1) Hiramatsu, H.; Yanagi, H.; Kamiya, T.; Ueda, K.; Hirano, M.; Hosono, H. Crystal structures, optoelectronic properties, and electronic structures of layered oxychalcogenides MCuOCh ($\text{M} = \text{Bi, La}$; $\text{Ch} = \text{S, Se, Te}$): effects of electronic configurations of M^{3+} ions. *Chem. Mater.* **2008**, *20*, 326.
- (2) Lany, S. Semiconductor thermochemistry in density functional calculations. *Phys. Rev. B* **2008**, *78*, 245207.
- (3) Stevanović, V.; Lany, S.; Zhang, X.; Zunger, A. Correcting density functional theory for accurate predictions of compound enthalpies of formation: Fitted elemental-phase reference energies. *Phys. Rev. B* **2012**, *85*, 115104.